



Universiteit
Leiden
The Netherlands

Observed polarized scattered light phase functions of planet-forming disks

Ginski, C.; Tazaki, R.; Dominik, C.; Stolker, T.

Citation

Ginski, C., Tazaki, R., Dominik, C., & Stolker, T. (2023). Observed polarized scattered light phase functions of planet-forming disks. *The Astrophysical Journal*, 953(1).
doi:10.3847/1538-4357/acdc97

Version: Publisher's Version
License: [Creative Commons CC BY 4.0 license](https://creativecommons.org/licenses/by/4.0/)
Downloaded from: <https://hdl.handle.net/1887/3716869>

Note: To cite this publication please use the final published version (if applicable).



Observed Polarized Scattered Light Phase Functions of Planet-forming Disks

Christian Ginski^{1,2,3} , Ryo Tazaki^{3,4,5} , Carsten Dominik³ , and Tomas Stolker¹ ¹ Leiden Observatory, Leiden University, PO Box 9513, 2300 RA Leiden, The Netherlands; christian.ginski@universityofgalway.ie² School of Natural Sciences, Center for Astronomy, University of Galway, Galway, H91 CF50, Ireland³ Anton Pannekoek Institute for Astronomy, University of Amsterdam, Science Park 904, 1098XH Amsterdam, The Netherlands⁴ Institute of Planetology and Astrophysics, Université Grenoble Alpes, F-38000 Grenoble, France⁵ Astronomical Institute, Graduate School of Science, Tohoku University, 6-3 Aramaki, Aoba-ku, Sendai 980-8578, Japan

Received 2023 January 11; revised 2023 June 6; accepted 2023 June 6; published 2023 August 7

Abstract

Dust particles are the building blocks from which planetary bodies are made. A major goal of studies of planet-forming disks is to constrain the properties of dust particles and aggregates in order to trace their origin, structure, and the associated growth and mixing processes in the disk. Observations of the scattering and/or emission of dust in a location of the disk often lead to degenerate information about the kinds of particles involved, such as the size, porosity, or fractal dimensions of aggregates. Progress can be made by deriving the full (polarizing) scattering phase function of such particles at multiple wavelengths. This has now become possible by careful extraction from scattered light images. Such an extraction requires knowledge about the shape of the scattering surface in the disk, and we discuss how to obtain such knowledge as well as the associated uncertainties. We use a sample of disk images from observations with the Very Large Telescope/SPHERE to, for the first time, extract the phase functions of a whole sample of disks with broad phase-angle coverage. We find that polarized phase functions come in two categories. Comparing the extracted functions with theoretical predictions from rigorous T-Matrix computations of aggregates, we show that one category can be linked back to fractal, porous aggregates, while the other is consistent with more compact, less porous aggregates. We speculate that the more compact particles become visible in disks where embedded planets trigger enhanced vertical mixing.

Unified Astronomy Thesaurus concepts: [Exoplanets \(498\)](#); [Planet formation \(1241\)](#); [Protoplanetary disks \(1300\)](#); [Circumstellar disks \(235\)](#); [High contrast techniques \(2369\)](#); [Direct imaging \(387\)](#); [Polarimetry \(1278\)](#)

1. Introduction

Gas- and dust-rich circumstellar disks are the sites of ongoing planet formation. However, the early stage of planet formation, such as the formation of planetesimals, remains a matter of discussion, as it comes with a number of barriers inhibiting grain growth and the formation of planetesimals (e.g., Brauer et al. 2008; Zsom et al. 2010; Birnstiel et al. 2012). The sizes and structures of growing dust aggregates are of crucial relevance to the barriers because these quantities influence the sticking and aerodynamic properties (Ormel et al. 2007; Zsom et al. 2010; Okuzumi et al. 2012; Kataoka et al. 2013; Krijt et al. 2016; Lorek et al. 2018; Garcia & Gonzalez 2020; Kobayashi & Tanaka 2021; Estrada et al. 2022). Thus, by determining these properties by disk observations, one can conclude the early planet formation and transport processes, including vertical mixing.

The past decade was revolutionary for resolved observations of young planet-forming disks in the near-infrared. Driven by advances in instrumentation, several large surveys have been conducted or are still ongoing, such as SEEDS (Tamura 2016), DARTTS-S (Avenhaus et al. 2018; Garufi et al. 2020), Gemini-LIGHTS (Rich et al. 2022), and SPHERE-DESTINYs (Ginski et al. 2021). A summary of the field was recently presented by Benisty et al. (2022). Due to these ongoing observational programs, more than 150 systems have now been observed in (polarized) near-infrared scattered light. A large diversity of

substructures has been discovered, such as rings, gaps, and spirals, which are typically associated with ongoing planet formation (see, e.g., Benisty et al. 2022). The analysis of the scattered light data has often focused on either the basic disk geometry, tracing illumination and shadowing (e.g., Garufi et al. 2022) as a function of disk aspect ratio and disk symmetry, or on the disk morphology (e.g., Garufi et al. 2018).

However, the appearance of these objects in (polarized) scattered light is also strongly dependent on the properties of the dust grains or aggregates in the upper disk atmosphere (see, e.g., Min et al. 2005). In particular, the scattering-angle-dependent amount of flux that we receive from the different regions of the disk, the so-called (polarized) scattering phase function, encodes dust grain and aggregate properties (Tazaki et al. 2019). While the extraction of polarized scattered light phase functions has been done for geometrically flat debris disks (e.g., Milli et al. 2017, 2019; Olofsson et al. 2020; Engler et al. 2023), it is less common for young gas-rich disks, due to their more complex geometry. So far, this has only been done for the disks around the Herbig stars HD 97048 (Ginski et al. 2016) and HD 100546 (Quanz et al. 2011; Stolker et al. 2016) in polarized light and the T Tauri star multiple system GG Tau (McCabe et al. 2002) in total intensity.

In this study, we gathered a sample of 10 disks for which the surface height profile has been determined in the literature from near-infrared scattered light observations. The sample is comprised of Herbig and T Tauri stars, with the earliest spectral type being the B9.5 star HD 34282 and the latest spectral type the M0 star IM Lup. The systems cover a range of ages, from 1.1 Myr (IM Lup; Avenhaus et al. 2018) to 12.7 Myr (MY Lup; Avenhaus et al. 2018). All systems had also already



Original content from this work may be used under the terms of the [Creative Commons Attribution 4.0 licence](#). Any further distribution of this work must maintain attribution to the author(s) and the title of the work, journal citation and DOI.

Table 1
Spectral Types and Dust Masses of our Sample Systems

| System | SpType | $M_{\text{dust}} (M_{\oplus})$ | References |
|------------------------|--------|--------------------------------|------------|
| RXJ 1615.3-3255 | K5 | 140 | (1), (12) |
| HD 163296 | A1 | 75 | (2), (3) |
| IM Lup | M0 | 54 | (1), (3) |
| LkCa 15 | K5.5 | 33 | (4), (3) |
| PDS 66 | K1.5 | 15 | (5), (3) |
| PDS 70 | K7 | 12 | (1), (3) |
| 2MASSJ18521730-3700119 | K4 | 13 | (6), (3) |
| V 4046 Sgr | K4 | 48 | (7), (10) |
| HD 34282 | B9.5 | 87 | (8), (11) |
| MY Lup | K0 | 53 | (1), (9) |

References: (1) Luhman (2022); (2) Sartori et al. (2003); (3) van der Marel & Mulders (2021); (4) Krolkowski et al. (2021); (5) Pecaute & Mamajek (2016); (6) Herczeg & Hillenbrand (2014); (7) Pecaute & Mamajek (2013); (8) Kharchenko (2001) (9); Mulders et al. (2017); (10) Martinez-Brunner et al. (2022); (11) Stapper et al. (2022); and (12) van der Marel et al. (2019).

been observed at (sub)millimeter wavelengths, which allowed the estimation of dust masses based on their continuum flux. Our sample spans roughly an order of magnitude between the lowest-mass disk around PDS 70 (13 M_{\oplus}) and the highest-mass disk in the RXJ 1615.3–3255 system (140 M_{\oplus}). A summary of all included systems with the appropriate references is given in Table 1. Due to the ring-shaped substructure in most of these disks, planet formation is thought to be ongoing. In particular, our study includes the PDS 70 system, in which two young planets have been detected inside the disk cavity (Keppler et al. 2018; Haffert et al. 2019), and the HD 163296 system, for which the presence of two wide separation planets has been inferred from Atacama Large Millimeter/submillimeter Array gas kinematic observations (Pinte et al. 2018; Teague et al. 2018). In the following section, we briefly describe the observational data. In Section 3, we discuss how the phase functions were extracted, while we discuss their interpretation in light of dust aggregate models in Section 4. We summarize our results in Section 5.

2. Observations and Data Reduction

All data sets used in our study have been obtained with the Very Large Telescope/SPHERE (Beuzit et al. 2019) and its near-infrared camera IRDIS (Dohlen et al. 2008). The instrument was operated in dual-beam polarization imaging mode (de Boer et al. 2020; van Holstein et al. 2020), in either J or H broadband filters, to obtain (linear) polarized scattered light images of the circumstellar disks in each system. An overview of the observation setup and conditions is given in Table 3 in Appendix A. In all cases, the innermost 92.5 mas around the stellar position were covered by the standard *YJH_S* apodized Lyot coronagraph (Carbillet et al. 2011) and are therefore inaccessible for the analysis. All data sets that are included in our study have been previously discussed in the literature. We give the relevant references in Table 2. The data reduction has in all cases been carried out with the public IRDAP (IRDIS Data reduction for Accurate Polarimetry; van Holstein et al. 2020) pipeline with default settings.⁶ This includes a full-model-based determination and removal of

instrumental polarization, as well as the measurement and subsequent subtraction of astrophysical stellar polarization.

3. Phase Function Extraction

To minimize the effect of multiple scattering on the extracted phase functions, we use in all cases the Q_{ϕ} images for the extraction. The Q_{ϕ} images are defined such that they contain only the azimuthal polarization component, relative to the central star, as positive signal (see Monnier et al. 2019 for a detailed description), i.e., the expected polarization orientation due to single scattering events. We discuss the remaining influence of multiple scattering in detail for the case of IM Lup in Tazaki et al. (2023).

3.1. Surface Height Profiles

The key challenge in extracting the scattered light phase function of young gas-rich disks is the uncertainty of the vertical structure. Here we are particularly interested at which height above the disk midplane the optical depth τ becomes equal to 1, i.e., the surface layer from which the majority of the disk scattered light originates. For ease of use within the further discussion, we will refer to this as the surface height of the disk within this study.⁷

While the surface height may generally be inferred from detailed radiative transfer modeling, there exists a subclass of disks for which it can be directly determined from the data themselves. As shown by de Boer et al. (2016) and Ginski et al. (2016), the disk surface height can be computed for disks with radial substructures, such as multiple rings. This is done by measuring the inclination of the ring and its offset along the minor axis from the central star position in the image. This directly gives the surface height at the ring location. If there are multiple rings, then the radial dependence of the disk surface height can be directly traced. Both of the mentioned studies found that the surface height profile for the two studied target systems (RXJ 1615 and HD97048) can be described reasonably well with a single power-law profile of the form:

$$H(r) = H_{\text{ref}} / (r_{\text{ref}} / 1\text{au})^{\alpha} * (r / 1\text{au})^{\alpha}, \quad (1)$$

where $H(r)$ is the radial-dependent surface height, H_{ref} is a reference height at reference separation r_{ref} (all in astronomical units), and α is the flaring exponent. Avenhaus et al. (2018) found that the surface height profile for five disks in their study could all be described by the same power-law profile with a flaring exponent of $\alpha = 1.22 \pm 0.03$. This indicates that for single-ringed disks, i.e., when only a surface height at a single radial separation is known, we may still infer a reasonable guess of the radial-dependent surface height profile by using the height measurement as a reference height in the power law and by assuming a standard flaring exponent of $\alpha = 1.22$. For our sample, we draw the surface profile parameters from the literature. For the RXJ 1615, IM Lup, and V 4046 Sgr multiring systems, we use the specific power-law profiles fitted by Avenhaus et al. (2018). For the HD 34282 multiring system, we likewise use the power-law profile given by de Boer et al. (2020). For the remaining single-ringed disks, we use the

⁶ <https://irdap.readthedocs.io>

⁷ We note that this is not identical to the pressure scale height of the disk, which is typically a factor 3–4 smaller than the scattered light surface height (Chiang et al. 2001).

Table 2
Values for the Surface Height Geometry of the Studied Disks

| System | | d (pc) | i ($^{\circ}$) | PA ($^{\circ}$) | $h/r_{\text{ref}}^{\alpha}$ | r_{ref} (au) | α | Ref. |
|------------------------|---------|-------------|-----------------------|----------------------|-----------------------------|--------------------------|----------|---------------|
| RXJ 1615.3-3255 | Nominal | 155.6 | 47.2 | 145.0 | 0.091 | 161.8 | 1.12 | (3) |
| | Min | | | | 0.140 | 162.3 | 1.02 | |
| | Max | | | | 0.059 | 161.3 | 1.22 | |
| HD 163296 | Nominal | 101.0 | 46.0 | 134.8 | 0.086 | 63.6 | 1.22 | (1), (2), (3) |
| | Min | | | | 0.081 | 68.7 | 1.19 | |
| | Max | | | | 0.090 | 58.6 | 1.25 | |
| IM Lup | Nominal | 155.8 | 55.0 | 325.0 | 0.046 | 149.6 | 1.27 | (3) |
| | Min | | | | 0.095 | 154.3 | 1.07 | |
| | Max | | | | 0.022 | 144.9 | 1.47 | |
| LkCa 15 | Nominal | 157.2 | 50 | 60 | 0.074 | 57.7 | 1.22 | (3), (4), (5) |
| | Min | | | | 0.059 | 60.1 | 1.19 | |
| | Max | | | | 0.089 | 53.7 | 1.25 | |
| PDS 66 | Nominal | 97.9 | 30.3 | 189.2 | 0.052 | 84.2 | 1.22 | (3) |
| | Min | | | | 0.055 | 84.7 | 1.19 | |
| | Max | | | | 0.050 | 83.5 | 1.25 | |
| PDS 70 | Nominal | 112.4 | 49.7 | 158.6 | 0.041 | 99.1 | 1.25 | (6), (7) |
| | Min | | | | 0.044 | 105.1 | 1.22 | |
| | Max | | | | 0.039 | 93.2 | 1.28 | |
| 2MASSJ18521730-3700119 | Nominal | 147.1 | 30 | 124 | 0.046 | 43.4 | 1.10 | (8) |
| | Min | | | | 0.065 | 45.2 | 1.00 | |
| | Max | | | | 0.034 | 41.6 | 1.20 | |
| V 4046 Sgr | Nominal | 71.5 | 32.2 | 74.7 | 0.017 | 26.7 | 1.61 | (3) |
| | Min | | | | 0.027 | 26.8 | 1.47 | |
| | Max | | | | 0.012 | 26.6 | 1.74 | |
| HD 34282 | Nominal | 308.6 | 57.0 | 118.0 | 0.064 | 86.4 | 1.35 | (9) |
| | Min | | | | 0.071 | 89.5 | 1.27 | |
| | Max | | | | 0.057 | 83.3 | 1.43 | |
| MY Lup | Nominal | 157.2 | 77.0 | 239.0 | 0.073 | 121.0 | 1.22 | (3) |
| | Min | | | | 0.073 | 125.8 | 1.19 | |
| | Max | | | | 0.072 | 116.3 | 1.25 | |

Notes. We give the nominal values used as well as the values for the minimal and maximal surface height that we considered. The references are: (1) Muro-Arena et al. (2018); (2) Isella et al. (2016); (3) Avenhaus et al. (2018); (4) Thalmann et al. (2014); (5) Thalmann et al. (2016); (6) Keppler et al. (2018); (7) Hashimoto et al. (2012); (8) Villenave et al. (2019); and (9) de Boer et al. (2021).

literature values for the surface heights of the rings as reference heights and the standard flaring exponent of $\alpha = 1.22$ by Avenhaus et al. (2018). For the RXJ1852 and PDS 70 systems, a different flaring exponent was inferred from radiative transfer modeling by Villenave et al. (2019) and Keppler et al. (2018), respectively, and we make use of their fitted values.

In order to capture the uncertainty of the extracted phase functions due to the uncertainty of the surface height, we always consider three scenarios for each system: (1) the nominal surface height profile; (2) a strongly “flared” profile; and (3) a “flat” profile. The flared and flat profiles consider the uncertainty of the reference height, the reference separation, and the flaring exponent. For the “flared” profile, we use the upper bound on the reference height, the lower bound on the reference separation, and the upper bound on the flaring exponent, while we switch the lower and upper bounds for each parameter for the “flat” profile. We summarize all profile parameters for each system in Table 2 and illustrate all three profiles (nominal, flared, and flat) for the RXJ 1615 system in the top panel of Figure 1. In the bottom panel of Figure 1, we show the corresponding deviations in scattering angle between the “flared” and “flat” surface profile extremes. While we see deviations of up to $\sim 5^{\circ}$ in the inner disk region, these are smaller in the outer disk. We note that the intermediate region between the inner disk and outer edge, which shows deviations

of less than 1° , is close to the reference separation for which the reference height was directly measured by Avenhaus et al. (2018). Thus, the deviation in this region is dominated by the (small) uncertainties of these quantities. We show similar figures for the maximum deviation of the scattering angle for our complete sample in Figure 7 in the Appendix B. Unsurprisingly, the largest deviations are found close to the outer disk edge for the systems with large uncertainties in their flaring exponent, i.e., IM Lup and HD 34282 in particular. In general, we are avoiding these outer disk regions for phase function extraction and typically consider regions for which the uncertainty in scattering angle is less than $\sim 10^{\circ}$, with the main exception being the two aforementioned systems. However, as we explain in the following section, we do for all systems incorporate the resulting deviations of the extracted phase functions between all three surface height profiles in their uncertainties.

3.2. Extraction with Diskmap

For the extraction of the phase functions, we use the publicly available diskmap Python package by Stolker et al. (2016).⁸ While the package is described in detail in Stolker et al. (2016), we give a brief summary here of the extraction steps. As

⁸ <https://diskmap.readthedocs.io>

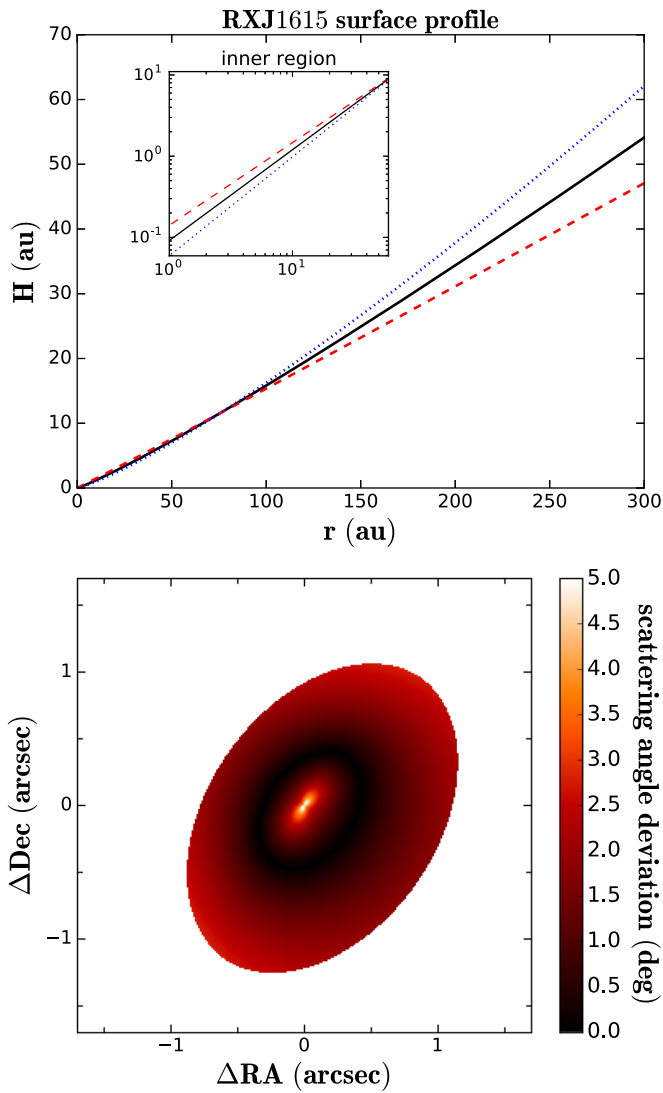


Figure 1. Top: exemplary $\tau = 1$ surface profile for the RXJ 1615 system, as used in our phase function extraction. The solid black curve indicates the nominal surface profile, while the blue dotted and red dashed curves indicate the flared and flat extremes, respectively. We consider these as the boundaries for the region of uncertainty. The inset shows the region inside 50 au on a log scale for clarity. Bottom: maximum deviation of the scattering angles between the flared and flat disk profiles for each position within the image of the RXJ 1615 system. We find the largest deviation of up to 5° close to the star and significantly smaller deviations farther out. Note that the dark region with the smallest deviations was used for normalization of the surface power-law profile.

described in the previous section, the $\tau = 1$ surface for all our system is described by a single power-law profile. Given this profile and the inclination of the disk, diskmap calculates for each pixel in the image the distance from the central star and subsequently the angle under which scattered light is received from this part of the disk. We show this for the RXJ 1615 system in Figure 2 (middle panel). The flux is corrected for the square-distance-dependent illumination dropoff and is then extracted for each pixel, giving a single data point for the polarized scattering phase function. These data points are then placed in bins of scattering angles with a width of 5° . For each bin, the median scattering angle of all the included pixels and the median flux is computed, giving the final data point for this angular bin. The standard deviation within each bin is used as a measure for the uncertainty of the phase function and captures

effects due to the width of the bin, as well as photometric uncertainties.

To include the uncertainty of the surface height profile, we repeat the extraction for the “flat” and the “flared” extreme cases and calculate for each angle bin the flux difference. We consider this difference as the uncertainty of the phase function introduced by the uncertainty of the surface height profile. We quadratically combine this uncertainty with the standard deviation in each bin for the nominal extraction and consider the result as the total uncertainty of the extracted phase function at each angle.

For each system, we selected extraction regions centered on known bright ring features. Since the surface height profile is directly measured at the ring locations, this minimizes the introduced uncertainty, while simultaneously selecting the region of the disk with the highest signal-to-noise ratio. If multiple rings are present, then we separately extracted the phase function for each ring. In Figure 2, we show the two selected extraction regions for the RXJ 1615 system. The extraction and individual phase functions for all systems are shown in Appendix B.

In Figure 3, we show the final extracted phase function for all systems and photometric bands. We note that in Figure 3, we show the average phase function for the IM Lup and V 4046 Sgr systems, instead of extractions for individual rings. For the HD 163296 and RXJ 1615 systems, we show phase functions after correction for azimuthal shadowing, as discussed in the following section.

3.3. Effects of Azimuthal Shadowing

An aspect that may complicate the extraction of the phase function in some systems is azimuthal shadowing, since it changes the brightness of the disk regions due to reduced illumination, an effect that needs to be separated from the phase function. There are now a number of known class II objects for which shadows are observed in scattered light (see Benisty et al. 2022 for an overview and detailed discussion). One of the most iconic systems is probably HD 142527 (Canovas et al. 2013; Avenhaus et al. 2014), for which the inner and outer disk are strongly misaligned (70° ; Marino et al. 2015), leading to two narrow shadows being projected on the outer disk. Such narrow and well-defined shadows are not of major concern for the extraction of the overall phase function, as the small region affected by the shadows can simply be excluded. However, as was shown for the HD 139614 system by Muro-Arena et al. (2020), small misalignments or warps in the disk can lead to very broad and somewhat diffuse shadowing, which covers in extreme cases an azimuthal range of more than 180° . For such systems, the problem is twofold. On the one hand, the exclusion of large azimuthal regions of the disk from the extraction may severely limit the range of scattering angles for which the phase function can be extracted. On the other hand, these shadows are less well defined, making it more difficult to decide which regions of the disk might be trusted for phase function extraction.

To estimate if the disks in our sample may be affected by broad shadowing effects, we performed a simple analysis. If there is no shadowing present and the brightness distribution of the disk structures is solely due to the dust scattering phase function,⁹ then we would expect the disk surface brightness to

⁹ We imply the following assumptions here: that there are no azimuthal variations in the dust grain size distribution or composition, that the disks are not eccentric, and that there are no or only small azimuthal variations in surface density.

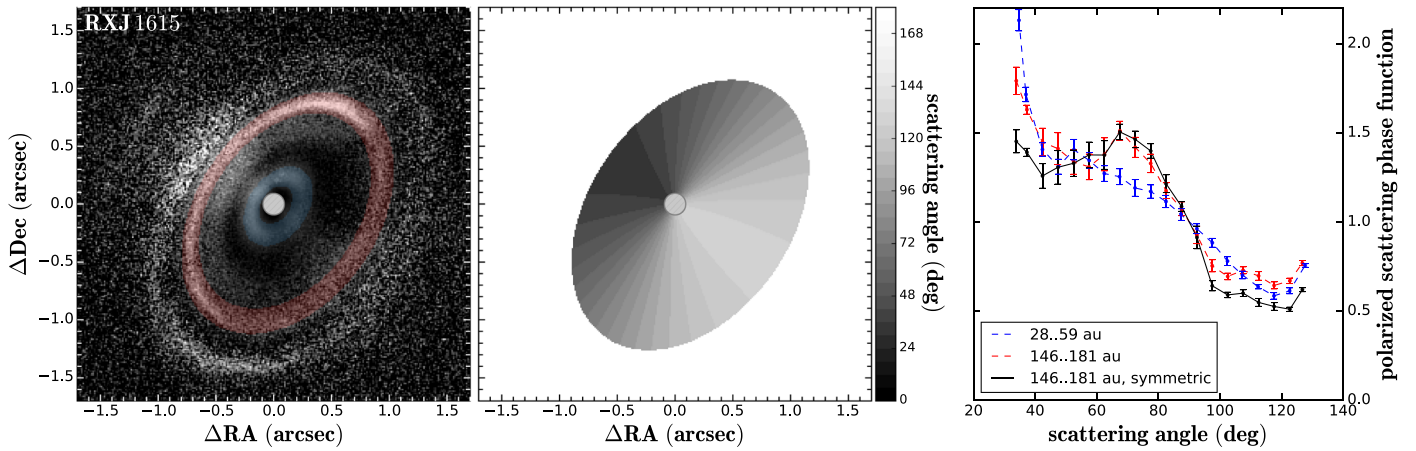


Figure 2. Extracted polarized scattered phase functions and extraction regions for the H -band data of the RXJ 1615 system. Left: H -band data of RXJ 1615 scaled with the square of the distance from the central star. The blue and red transparent overlays highlight the two regions used for phase function extraction, i.e., the inner disk region close to the coronagraph and the bright outer ring. Middle: position-dependent scattering angles calculated with the nominal surface height profile of the system. Right: extracted phase functions for the inner disk region (blue dashed line), the outer ring (red dashed line), and an azimuthal region of 180° centered on the northwestern ansae of the outer ring (black solid line), which should be less affected by azimuthal shadowing.

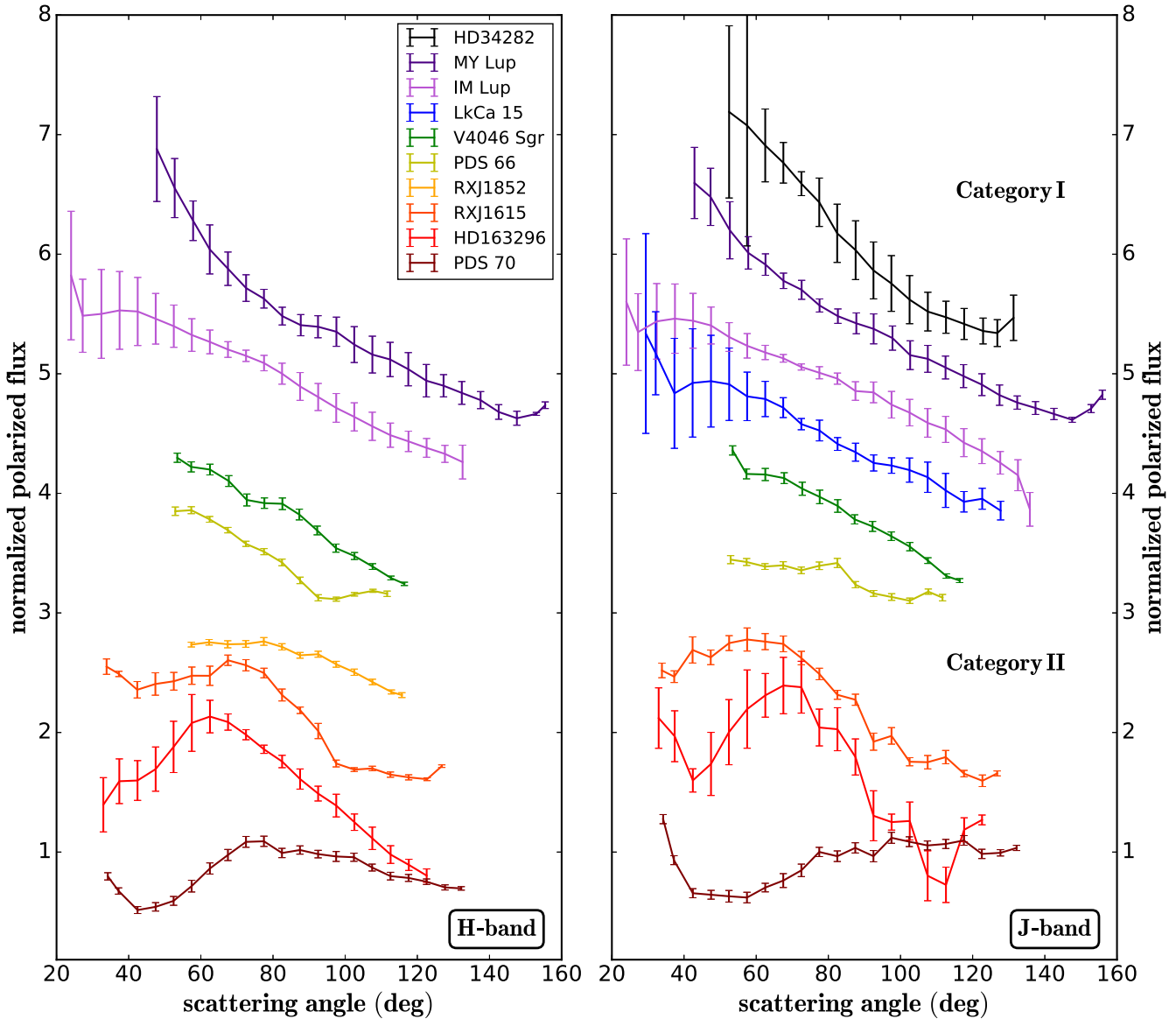


Figure 3. Final extracted polarized scattered light phase functions for all targets in our sample. We show the H -band data on the left and the J -band data on the right. All phase functions were normalized at scattering angles of 90° and had an arbitrary offset applied for better visibility. The colors indicate the same systems in both panels, and the order of the phase functions from top to bottom is the same as indicated in the legend. Note that both H and J band were not available for all targets.

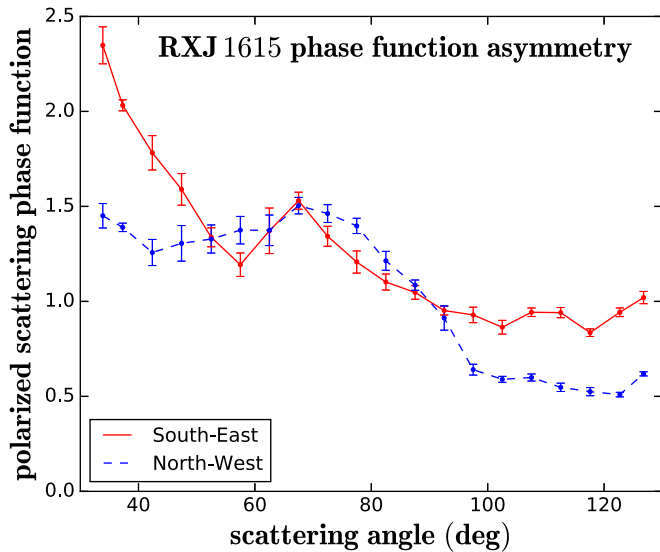


Figure 4. Polarized scattered phase functions of the RXJ 1615 H -band data extracted from the brightest ring in the data set between projected separations of 146 and 181 au. The blue dashed phase function was extracted from an azimuthal region of 180° centered on the northwest ansae of the disk, while the red solid curve was extracted from a region centered on the southeast ansae. Both phase functions were normalized at scattering angles of 90° . The differences may be explained by azimuthal shadowing of the extraction region due to an inner disk component, which strongly affected the southwestern region.

be axis-symmetric relative to the disk minor axis. Thus, for all our systems, we flipped the disk images around the minor axis and then divided the original image by the flipped image. This indicates the brightness ratio between the two “mirrored” sides of the disk. We show the axis-symmetric brightness ratio for all systems in the appendix in Figure 17. For most systems, the deviation in brightness is smaller than a factor ~ 2 , with the notable exceptions of the RXJ 1615 system (up to factor ~ 4), the HD 163296 system (up to factor ~ 5), and the HD 34282 system (up to factor ~ 6). We thus consider that the RXJ 1615 and HD 163296 systems may be affected by broad shadowing. This was in fact discussed for both systems in the literature by de Boer et al. (2016) and Muro-Arena et al. (2018), respectively. In the case of HD 34282, de Boer et al. (2021) discuss a possible spiral within the disk, thus in this case we may instead trace a genuine azimuthal asymmetry in the dust surface density rather than shadowing effects.

To give an indication how strongly these shadowing effects may affect the extracted phase function, we performed two separate extractions for the RXJ 1615 system, choosing the bright ring between deprojected radii of 146 au and 181 au. One extraction only considered the brighter northwest side of the disk, while the second extraction only considered the fainter southeast side, i.e., the side of the ring more strongly affected by shadowing. The results are shown in Figure 4 (both phase functions were normalized at scattering angles of 90°). While the profiles somewhat match between 60° and 90° , they deviate significantly at larger and smaller scattering angles. In particular, the phase function extracted from the southeast half of the disk shows more relative flux in both ranges. If we consider that the shadow is centered on the southeast ansae, this might be explained by the stronger shadowing close to 90° scattering angles or, put in a different way, the disk may rise out of the shadow at regions seen under small and large scattering angles.

We note that there is no geometric reason why the disk should specifically be warped or misaligned around the minor axis. In practice, there will in fact most likely be a deviation between the disk minor axis (defined by our arbitrary viewing geometry) and the warp or misalignment axis around which the disk tilts as a function of radial separation from the central star. However, if the axis of misalignment were closer to the disk major axis, then one would not expect a strong brightness asymmetry between the two disk ansae, as seen in Figure 17. de Boer et al. (2016) also noted that the brightness asymmetry seemed to switch sides between subsequent ring structures in the disk, i.e., in the next outer (overall fainter) ring, the southeast ansae is brighter than the northwest ansae, indicating a continuous warp in the disk. If the disk near or far side were strongly affected by this effect, then one may expect strong changes in brightness asymmetries between the disk near and far side seen in subsequent rings. This does however not seem to be the case. We can thus conclude that the broad shadowing effect is likely centered at least near the disk ansae. This is further supported by the fact that the phase function extracted from the southeast side of the disk, shown in Figure 4, increases the relative flux level toward both the forward- and back-scattering sides of the disk. If the shadow were not centered close to the southeast ansae, then we would naively expect either a steeper phase function relative to the northeast at larger scattering angles or a flatter phase function at small scattering angles.

Given our analysis, we thus consider the phase function extracted from the northwest side of the disk in the RXJ 1615 system to be minimally or in any case less affected by shadowing and use it for further analysis and comparison to other systems. This phase function is shown as the black solid line in Figure 2 (named “symmetric” in the legend, as this is the phase function of the point-symmetric version of this disk relative to the minor axis). For the HD 163296 system, we then follow the same strategy and choose the northwest side of the disk for phase function extraction, as it appears less affected by shadowing compared to the southeast.

For the HD 34282 system, the situation is different, as the detected asymmetry likely traces a genuine asymmetry in the dust surface density profile, possibly due to spiral density waves in the disk gas. It is then not clear which regions may be best suited to extracting an unbiased scattering phase function. We thus include in this case the full azimuthal range in the extraction and caution that a more detailed analysis of the system with dedicated radiative transfer modeling should be performed in the future, to revise our preliminary results.

3.4. Limb Brightening

In addition to shadowing effects, the shape of the phase function may be influenced by the viewing geometry. In recent studies of optically thin debris disks, Olofsson et al. (2020) and Engler et al. (2023) found that the relative flux extracted at $\sim 90^\circ$ scattering angles, i.e., close to the disk ansae, may be enhanced compared to the intrinsic phase function of the present dust particles, due to a higher column density along the line of sight. This effect is sometimes referred to as “limb brightening” (Engler et al. 2023). The systems in our sample are all at an earlier evolutionary stage before the gas dispersal in the disk, and it is generally assumed that they are optically thick at near-infrared wavelengths (Chiang & Goldreich 1997). Thus, we do not expect that the column density along the line

of sight will change significantly for different scattering angles. However, due to the flaring surface height profiles of these systems, we may instead expect an artificial increase in the flux ratio between the disk forward- and back-scattering sides, i.e., between small and large scattering angles. At small scattering angles (on the disk near side), the line of sight encompasses more of the illuminated disk surface than is the case for large scattering angles (on the disk far side). We discuss this effect in detail for the IM Lup system in Tazaki et al. (2023). Using radiative transfer models, we found in this study that the effect depends on the inclination, the local aspect ratio, and the flaring exponent of the disk surface height profile. For the specific case of the IM Lup system, this may introduce a $\sim 25\%$ brightening for scattering angles smaller than $\sim 50^\circ$. However, we caution that this strongly depends on the dust composition, i.e., for dust with high scattering albedos, limb brightening may be much smaller or even insignificant, because multiple scattering reduces the polarized flux at smaller scattering angles and starts to (at least partly) counteract this effect. Dedicated radiative transfer modeling is required to determine the influence of this effect for individual systems.

In a more general sense, this limb-brightening effect will typically not strongly alter the shape of the phase functions for optically thick disks, such as the ones discussed in our current study. Rather, it will slightly increase the slope of the overall phase functions. We note that there may be one exception to this, which is the MY Lup system, which is seen under a particularly high inclination of 77° . The extracted phase function in Figure 3 is strongly peaked toward small scattering angles. Based on the results in Tazaki et al. (2023), we find it likely that the intrinsic phase function of dust particles in MY Lup has a significantly smaller slope, possibly with no upturn at small scattering angles. As we summarize in Table 2, the remaining systems in our study have either a comparable inclination to IM Lup (this is the case for HD 34282) or are seen under significantly smaller inclination. Thus, while the effect should be considered for future detailed modeling of individual systems, it will not strongly affect the general population level trends that we recover.

4. Results and Discussion

4.1. Qualitative Inference of Dust Properties

Figure 3 shows that the extracted polarization phase functions are diverse in terms of their shapes. The shapes can be roughly divided into two categories: those that are monotonically increasing in polarized flux with decreasing scattering angle (category I: e.g., HD 34282, MY Lup, IM Lup, LkCa 15, and V4046 Sgr) and those that turnaround at a scattering angle of 60° – 80° , go through a local minimum, and then increase again at the smallest scattering angles (category II: e.g., HD 163296 and PDS 70).¹⁰

To illustrate the origins of these variations, we perform T -matrix light-scattering calculations for various dust aggregates (Tazaki & Dominik 2022; see also Appendix C). The scattering matrix elements ($-S_{12}$ in Bohren & Huffman 1983) obtained by the simulations are summarized in Figure 5. There is a caveat when comparing the scattering matrix element and the observed phase function: a planet-forming disk is optically

thick in the near-infrared, and the scattering-angle dependence of the observed polarization flux might have been affected by radiative transfer effects, such as multiple scattering within the disk surface and limb brightening (see the detailed discussion of these effects in Tazaki et al. 2023). To distinguish it from the one extracted from an observed image, we will refer to the computed scattering matrix element as the intrinsic polarization phase function. While a three-dimensional radiative transfer calculation is necessary to determine the dust parameters more accurately from the extracted polarization phase function, it is possible to capture the general trend from the intrinsic phase function and infer the origins of the variations in the shape shown in Figure 3. In this context, we note that the back-scattering behaviors of the theoretical curves are similar to each other, because large-angle scattering is particularly sensitive to small-scale structures of aggregates (as small as the length scale of each monomer; see, for example, Figure 7 in Tazaki et al. 2016). In each panel of Figure 5, the same monomer model is used for different aggregates (see Appendix C), which leads to similarities in the back-scattering pattern.

Figure 5(a) illustrates how the intrinsic polarization phase function of aggregates varies with their size. The scattering-angle dependency of the polarized intensity is the result of the dependence of the two quantities overlapping: the total intensity phase function and the degree of linear polarization. When the aggregates are small compared to the wavelength, the scattered light distribution will be close to isotropic in total intensity, but the degree of polarization approaches 0 in the forward-scattering direction. As a result, the intrinsic polarization phase function turns around at an angle of scattering around 90° (for the case of pure Rayleigh scattering, the intrinsic polarization function is proportional to $1 - \cos^2 \theta$; see Bohren & Huffman 1983). As the aggregates become larger, the forward scattering in total intensity develops and compensates for the decrease in the degree of polarization. Consequently, the turnaround position shifts to the small-angle side.

Except for RXJ1852, none of the observed phase functions presented in Figure 3 exhibit the Rayleigh-scattering-like profile. This indicates that the aggregates have grown to at least micron sizes in those disks. For RXJ1852, the function appears to have a peak in polarized flux around a scattering angle of 80° , and the profile may be consistent with the presence of small, submicron-sized aggregates. Since the presence of such small particles makes the disk scattered light bluish (Tazaki et al. 2019), future multicolor observations would be useful to draw a conclusion.

The shape diversity in polarization phase functions could be resulting from a diversity of the structure and porosity of micron-sized aggregates. First of all, we focus on category I (the top six curves in the J band); all show monotonically increasing polarizing flux with decreasing scattering angle. In particular, the curves for V4046 Sgr, LkCa 15, and IM Lup seem to have approximately constant slopes, while the slopes of the curves for MY Lup and HD 34282 become steeper at scattering angles below 80° . Figure 5(b) demonstrates that aggregates with different fractal dimensions can explain these differences. Aggregates with a low fractal dimension (around 1.9) exhibit nearly constant slopes, except for scattering angles below 30° , whereas aggregates with a high fractal dimension (around 3.0) show a similar slope to fractal aggregates in the large scattering-angle region, but the slope

¹⁰ We note that in order to distinguish between these two categories, scattering angles smaller than 60° need to be covered, which translates to an approximate minimum inclination of 30° .

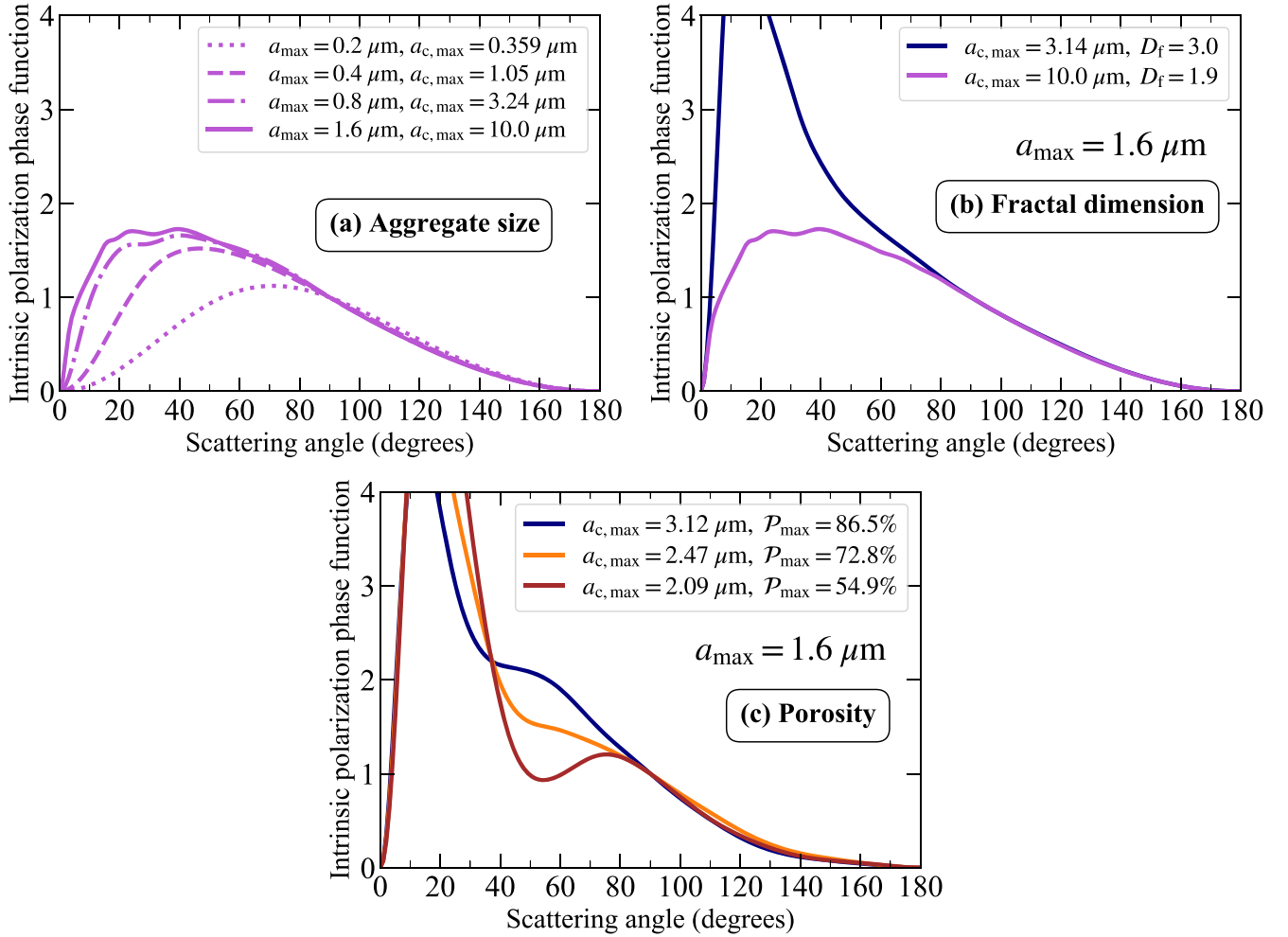


Figure 5. The effects of aggregate size, fractal dimension, and porosity on the intrinsic polarization phase function. The phase functions are normalized to a scattering angle of 90° . (a) The intrinsic functions for BCCA aggregates for various radii. The monomer radius is set as $a_{\text{mon}} = 0.1 \mu\text{m}$. The \mathcal{P}_{\max} values range from 82.7% to 99.6% from the smallest to largest aggregate, and as the size grows, a fractal dimension approaches 1.9. (b) The blue and violet lines represent the results for BPCA ($a_{c,\max} = 3.14 \mu\text{m}$, $D_f = 3.0$, $\mathcal{P}_{\max} = 86.8\%$) and BCCA ($a_{c,\max} = 10.0 \mu\text{m}$, $D_f = 1.9$, $\mathcal{P}_{\max} = 99.6\%$) aggregates, respectively. In these computations, we used $a_{\max} = 1.6 \mu\text{m}$ and $a_{\text{mon}} = 0.1 \mu\text{m}$. (c) The blue, orange, and brown lines represent the results for BPCA ($a_{c,\max} = 3.12 \mu\text{m}$, $\mathcal{P}_{\max} = 86.5\%$), BAM1 ($a_{c,\max} = 2.47 \mu\text{m}$, $\mathcal{P}_{\max} = 72.8\%$), and BAM2 ($a_{c,\max} = 2.09 \mu\text{m}$, $\mathcal{P}_{\max} = 54.9\%$) aggregates, respectively. Those aggregates have a fractal dimension close to three. In these computations, we used $a_{\max} = 1.6 \mu\text{m}$ and $a_{\text{mon}} = 0.4 \mu\text{m}$.

becomes steeper in the small scattering-angle region. Therefore, the approximately constant slopes observed in V4046 Sgr, LkCa 15, and IM Lup may be explained by fractal aggregates. In fact, the detailed radiative transfer calculations by Tazaki et al. (2023) showed that fractal aggregates best explain the observed phase function of the IM Lup disk. On the other hand, the phase functions for MY Lup and HD 34282 point to the presence of aggregates with a high fractal dimension, although the porosity is still high ($\sim 87\%$), unless the limb brightening is responsible for the steepening of the slope. Therefore, these disks might contain highly porous aggregates, although full radiative transfer modeling is needed to determine the fractal dimension.

Category II exhibits peculiar phase functions (e.g., RXJ 1615, HD 163296, and PDS 70 in Figure 3). First, there is a turnaround at scattering angles of 60° – 80° , and second, the polarized flux increases again at the smallest scattering angles. A similar trend has also been reported in the disk around HD 100546 (Stolker et al. 2016). The effects of radiative transfer within the disk surface would not account for this trend, as long as the disk structure is axisymmetric and is uniformly

illuminated by the central star. For example, multiple scattering tends to decrease the polarization flux on the forward-scattering side, but its dependency is monotonic and would not explain the rise at the smallest scattering angles (Tazaki et al. 2023). If this is the case, the tendency has to be attributed to the intrinsic properties of dust particles. However, the high-porosity aggregates that are thought to explain category I do not show such a tendency, as already shown in Figures 5(a) and (b). This means that the dust particles in these systems are different from the ones in category I.

One possibility is low-porosity aggregates (consisting of at least micron-sized grains). Figure 5(c) shows that a turnaround at scattering angles around 80° and a rise in polarization flux at small scattering angles appear simultaneously when the porosity is as low as $\sim 55\%$. Since this feature is not prominent for higher porosity, it seems to be triggered by an increased contribution of monomer–monomer electromagnetic interaction, as the monomers get packed closely for lower porosity. Therefore, the phase functions for the disks around HD 163296, PDS 70, and perhaps RXJ1615 might be explained by low-porosity aggregates. Low-

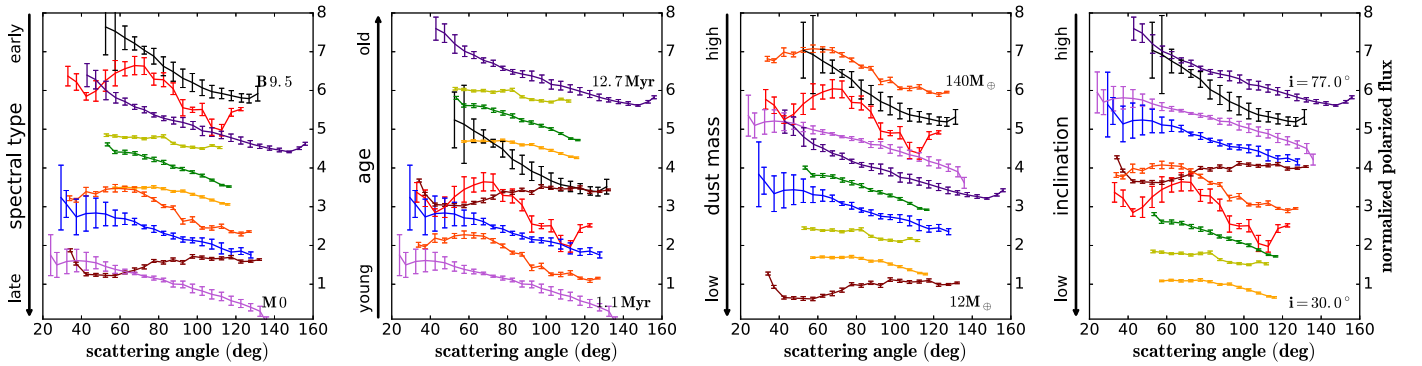


Figure 6. Phase functions for all 10 target systems ordered by various system parameters. We show the J -band data for all systems but one, since it is more complete. For the RXJ 1852 system, we show the H -band data, as there are no J -band observations of this system. The color code is the same as in Figure 3 for all systems. We indicate for each panel on the left y-axis the system parameter by which the phase functions were sorted and we indicate the extreme values of these parameters in the plot.

porosity aggregates tend to show a reddish polarized intensity color ($J/H < 1.0$; Tazaki et al. 2019). For RXJ 1615, Avenhaus et al. (2018) found that $J/H = 0.78 \pm 0.42$, thus indeed the disk appears red, i.e., is brighter in the H band relative to the central star than in the J band. We repeated an analog measurement to that described in Avenhaus et al. (2018) for the HD 163296 and the PDS 70 systems. We found $J/H = 0.75 \pm 0.11$ and $J/H = 0.94 \pm 0.21$ for HD 163296 and PDS 70, respectively. Thus, the polarized intensity colors for all three systems are consistent with the presence of low-porosity aggregates in the surface layers of the disk (although we caution that in the cases of RXJ 1615 and PDS 70, the error bars are large on the color measurement).¹¹

Low-porosity aggregates have relatively small area-to-mass ratios (i.e., weak dynamical coupling with gas), making them prone to settling on the disk midplane. For example, the Stokes number of a fractal aggregate with 0.1 micron monomers (Ballistic Cluster–Cluster Aggregation, or BCCA) and a compact spherical particle without porosity can differ by a factor of ~ 6 at $a = 1 \mu\text{m}$, where a is the volume-equivalent radius (Minato et al. 2006; Tazaki 2021). Efficient vertical mixing would thus be necessary to keep these aggregates in the disk surface layers (e.g., Mulders et al. 2013; Tazaki et al. 2021). Interestingly, the disks around HD 163296, PDS 70, and HD 100546 (studied in Stolker et al. 2016) have been suggested to host a planet in the disk (Quanz et al. 2013; Currie et al. 2014; Keppler et al. 2018; Teague et al. 2018; Casassus & Pérez 2019; Haffert et al. 2019). The presence of planets has been suggested to influence the vertical mixing of dust particles in disks by meridional circulation (Bi et al. 2021; Binkert et al. 2021; Szulágyi et al. 2022). Therefore, we speculate that the presence of planets might indirectly affect the dust properties at the disk surface, which might in turn explain the distinct phase functions from the others.

4.2. Trends with System Properties

As discussed in Section 4.1, we find an empirical dichotomy in the shape of the phase functions indicating different dust aggregate porosities. In order to find possible trends with basic system parameters, we plot the phase functions of all systems in order of stellar spectral type, system age, disk dust mass, and

disk inclination in Figure 6. For the stellar spectral type and the disk dust mass, we do not see any correlation between the two different categories of phase functions. For the system age, we notice that the three disks with lower dust porosities are among the younger sources in our sample, with ages of 5.4 Myr for PDS 70 (Müller et al. 2018), 5.1 Myr for HD 163296 (Alecian et al. 2013), and 1.4 Myr for RXJ 1615 (Wahhaj et al. 2010). However, the presumably youngest source in our sample, IM Lup (1.1 Myr; Avenhaus et al. 2018), is again part of the higher-porosity category. We stress that our sample is small and that individual system ages are inherently uncertain, thus an expanded study with a large number of systems will be needed to confirm if such a trend indeed exists.

In the rightmost panel of Figure 6, we order the phase functions by disk inclination. Here, we find that the two phase functions with a monotonous slope and strong forward-scattering peak were extracted from the two systems with the highest inclination in our study, i.e., MY Lup (77°) and HD 34282 (57°). Conversely, the two phase functions for the systems with the lowest inclination show a monotonous and shallow slope, with no indication for a similar forward-scattering peak (although we note that in these cases, the smallest scattering angles could not be sampled). This trend with inclination may well correspond to the limb-brightening effect discussed in Section 3.4.

4.3. Multiringed Systems

For three systems with multiple ringlike features, we were able to extract the polarized phase function at multiple separations: RXJ 1615, IM Lup, and V 4046 Sgr.

For RXJ 1615, we extracted the phase function from the innermost resolved ring between 28 au and 59 au, as well as the brightest full ring at a radial separation between 146 au and 181 au. The resulting extractions in the H band are shown in Figure 2. For comparison, we consider the extraction of the outer ring, which was corrected for azimuthal shadowing as discussed in Section 3.3 (the black solid curve in Figure 2). The two phase functions show very different shapes. While the outer disk shows the previously mentioned peak between 60° and 80° , the phase function of the inner disk zone is well described by a single slope for angles between 40° and 120° , but shows strong peaks at larger and smaller angles. Both of them seem to favor compact aggregates that have relatively high fractal dimensions, e.g., the Ballistic Particle–Cluster Aggregation (BPCA) aggregates shown in Figure 5(b). In order

¹¹ We note that we give all colors as defined by Avenhaus et al. (2018), i.e., $J/H = \frac{L_{\text{disk},J}/L_{\star,J}}{L_{\text{disk},H}/L_{\star,H}}$.

to explain the dip, the porosity needs to be relatively low, e.g., $\mathcal{P}_{\max} \sim 55\%$, at least for the outer region (Figure 5(c)). Since the phase functions are very different from each other, the inner and outer disk surfaces are likely dominated by different types of compact dust aggregates. As we have already discussed in the previous section, the presence of low-porosity aggregates in the upper disk atmosphere may indicate the presence of a perturber that leads to more efficient vertical mixing. This also fits well with our discussion in Section 3.3, which indicates that there is a warp present in the outer disk of the RXJ 1615 system, consistent with previous results by de Boer et al. (2016).

We discuss the IM Lup system in great detail in Tazaki et al. (2023). As a brief summary, we note that the two innermost disk zones between 70 and 110 au and between 130 and 170 au are well consistent with each other (see Figure 10). The outermost extraction zone between 217 and 257 au shows a much shallower slope toward small scattering angles (but also has intrinsically much larger uncertainties, due to the less-well-defined surface height profile in the outer disk; see Figure 7). As we argue in Tazaki et al. (2023), this may simply be an indication that the outer disk region is not well described anymore by the same power-law profile as the inner regions, due to decreasing surface density and thus decreasing optical depth.

The V 4046 Sgr system has arguably the most well-defined dual ring structure of all the disks in this study and shows no indication of significant azimuthal shadowing. We extracted the phase function from the inner region between 11 and 19 au, as well as from the outer ring between 23 and 34 au (see Figure 12). We find that both phase functions are well consistent with each other for angles larger than $\sim 80^\circ$, while the inner disk shows a slightly (but significantly) smaller slope for smaller scattering angles. It is unclear if this slight difference is due to the intrinsic phase functions in the inner and outer ring (thus indicating slightly different aggregate properties) or if it can be attributed to observational effects, such as limb brightening. Indeed, due to the steeper slope in the outer ring of the flared disk surface, we would expect a slightly stronger limb-brightening effect for the outer ring, which may then explain the small deviations between the two observed phase functions.

5. Summary

We measure for the first time the polarized scattering phase functions of 10 young planet-forming disks observed in the near-infrared. We find that even though the geometry of these disks is complex, phase functions with meaningful uncertainties can be extracted. While detailed radiative transfer models for individual systems are required to disentangle observational effects, such as limb brightening or azimuthal shadowing from the intrinsic phase function of the dust particles, we can still infer some general trends from the extracted phase functions.

1. We find empirically two distinct categories of phase functions. Category I has a monotonous slope, while category II displays a local maximum between 60° and 80° .
2. Disks in category I have phase functions consistent with micron-sized, high-porosity aggregates, while disks in category II require micron-sized, low-porosity aggregates to explain their phase function.

3. Category II disks appear consistent with red polarized intensity colors between the J/H bands, as predicted for micron-sized, low-porosity aggregates.
4. While we do not find general correlations with basic system parameters for the two phase function categories, we do note that category II disks include the HD 163296 and PDS 70 systems, both of which host embedded planets. Furthermore the literature data for the HD 100546 system, which is also suggested to host planets, is consistent with phase function category II.
5. If the presence of low-porosity aggregates is an indication for the presence of embedded planets, then this may indicate that the RXJ 1615 system, which also belongs to the category II disks, hosts an embedded planet similar to the cases of PDS 70 and HD 163296.

As further near-infrared observations of young disks become available, it will be most interesting to repeat the extraction performed for the small sample in this study, to investigate if the two tentative categories that we identify are indeed present in the larger population.

Acknowledgments

C.G. dedicates this work to the memory of Gisela Else Mäder. Her many years of selfless support enabled his past and present scientific work. The authors would like to thank the anonymous referee who helped to significantly improve the clarity of the manuscript. C.G. acknowledges funding from the Netherlands Organisation for Scientific Research (NWO) TOP-1 grant as part of the research program “Herbig Ae/Be stars, Rosetta stones for understanding the formation of planetary systems,” project No. 614.001.552. R.T. acknowledges the JSPS overseas research fellowship. R.T. also thanks Daniel Mackowski for making the MSTM codes publicly available. R.T. would also like to thank Bruce Draine for the availability of particle data of BA, BAM1, and BAM2, and Yasuhiko Okada for providing a generation code for BCCA. SPHERE is an instrument designed and built by a consortium consisting of IPAG (Grenoble, France), MPIA (Heidelberg, Germany), LAM (Marseille, France), LESIA (Paris, France), Laboratoire Lagrange (Nice, France), INAF—Osservatorio di Padova (Italy), Observatoire de Genève (Switzerland), ETH Zurich (Switzerland), NOVA (The Netherlands), ONERA (France), and ASTRON (The Netherlands), in collaboration with ESO. SPHERE was funded by ESO, with additional contributions from CNRS (France), MPIA (Germany), INAF (Italy), FINES (Switzerland), and NOVA (The Netherlands). SPHERE also received funding from the European Commission Sixth and Seventh Framework Programmes as part of the Optical Infrared Coordination Network for Astronomy (OPTICON), under grant No. RII3-Ct2004-001566 for FP6 (2004–2008), grant No. 226604 for FP7 (2009–2012), and grant No. 312430 for FP7 (2013–2016). This research has used the SIMBAD database, operated at CDS, Strasbourg, France (Wenger et al. 2000). We used the Python programming language,¹² especially the SciPy (Virtanen et al. 2020), NumPy (Oliphant 2006), Matplotlib (Hunter 2007), and astropy (Astropy Collaboration et al. 2013, 2018) packages. We thank the writers of these software packages for making their work available to the astronomical community.

¹² Python Software Foundation, <https://www.python.org/>.

Facility: VLT(SPHERE).

Software: MSTM v3.0 (Mackowski & Mishchenko 2011).

Appendix A

Summary of Observation Setups and Conditions. In Table 3 we summarize the observing, setup, and conditions for all data sets used in this study.

Appendix B

Phase Function Extraction of all Systems. In the following we show summary figures for the phase function extraction of all systems. In Figure 7 we show the maximum deviation of the scattering angles based on different surface height profiles. In Figures 8 to 16 we show the individual phase function extractions for each system. Finally in Figure 17 we highlight possible asymmetries due to non-azimuthal disk geometry or shadowing.

Table 3
Observing Dates, Instrument Setup, and Weather Conditions for All Systems in Our Study

| Target | Date | Filter | DIT (s) | # Frames | Seeing (arcsec) | τ_0 (ms) | ESO ID |
|------------------------|------------|--------|---------|----------|-----------------|---------------|----------------|
| RXJ 1615.3-3255 | 14-03-2016 | BB_H | 64 | 80 | 1.1 | 2.6 | 096.C-0523(A) |
| | 14-03-2016 | BB_J | 64 | 48 | 1.1 | 2.2 | 096.C-0523(A) |
| HD 163296 | 26-05-2016 | BB_H | 8 (16) | 64 (64) | 1.0 | 2.8 | 097.C-0523(A) |
| | 26-05-2016 | BB_J | 16 | 200 | 0.8 | 2.0 | 097.C-0523(A) |
| IM Lup | 13-03-2016 | BB_H | 64 | 48 | 1.3 | 3.4 | 096.C-0523(A) |
| | 11-03-2016 | BB_J | 64 | 56 | 0.9 | 1.5 | 096.C-0523(A) |
| LkCa 15 | 19-12-2015 | BB_J | 32 | 120 | 0.7 | 2.4 | 096.C-0248(A) |
| PDS 66 | 15-03-2016 | BB_H | 64 | 56 | 0.9 | 2.8 | 096.C-0523(A) |
| | 14-03-2016 | BB_J | 64 | 48 | 1.1 | 2.5 | 096.C-0523(A) |
| PDS 70 | 09-08-2019 | BB_H | 64 | 36 | 1.5 | 2.1 | 0102.C-0916(B) |
| | 26-03-2016 | BB_J | 64 | 52 | 1.9 | 1.3 | 096.C-0333(A) |
| 2MASSJ18521730-3700119 | 15-05-2017 | BB_H | 64 | 12 | 1.2 | ... | 099.C-0147(B) |
| V 4046 Sgr | 13-03-2016 | BB_H | 64 | 48 | 1.0 | 2.3 | 096.C-0523(A) |
| | 12-03-2016 | BB_J | 64 | 48 | 1.5 | 1.7 | 096.C-0523(A) |
| HD 34282 | 19-12-2015 | BB_J | 64 | 88 | 0.6 | 3.0 | 096.C-0248(A) |
| MY Lup | 15-03-2016 | BB_H | 64 | 40 | 0.7 | 3.7 | 096.C-0523(A) |
| | 15-03-2016 | BB_J | 64 | 35 | 0.9 | 2.4 | 096.C-0523(A) |

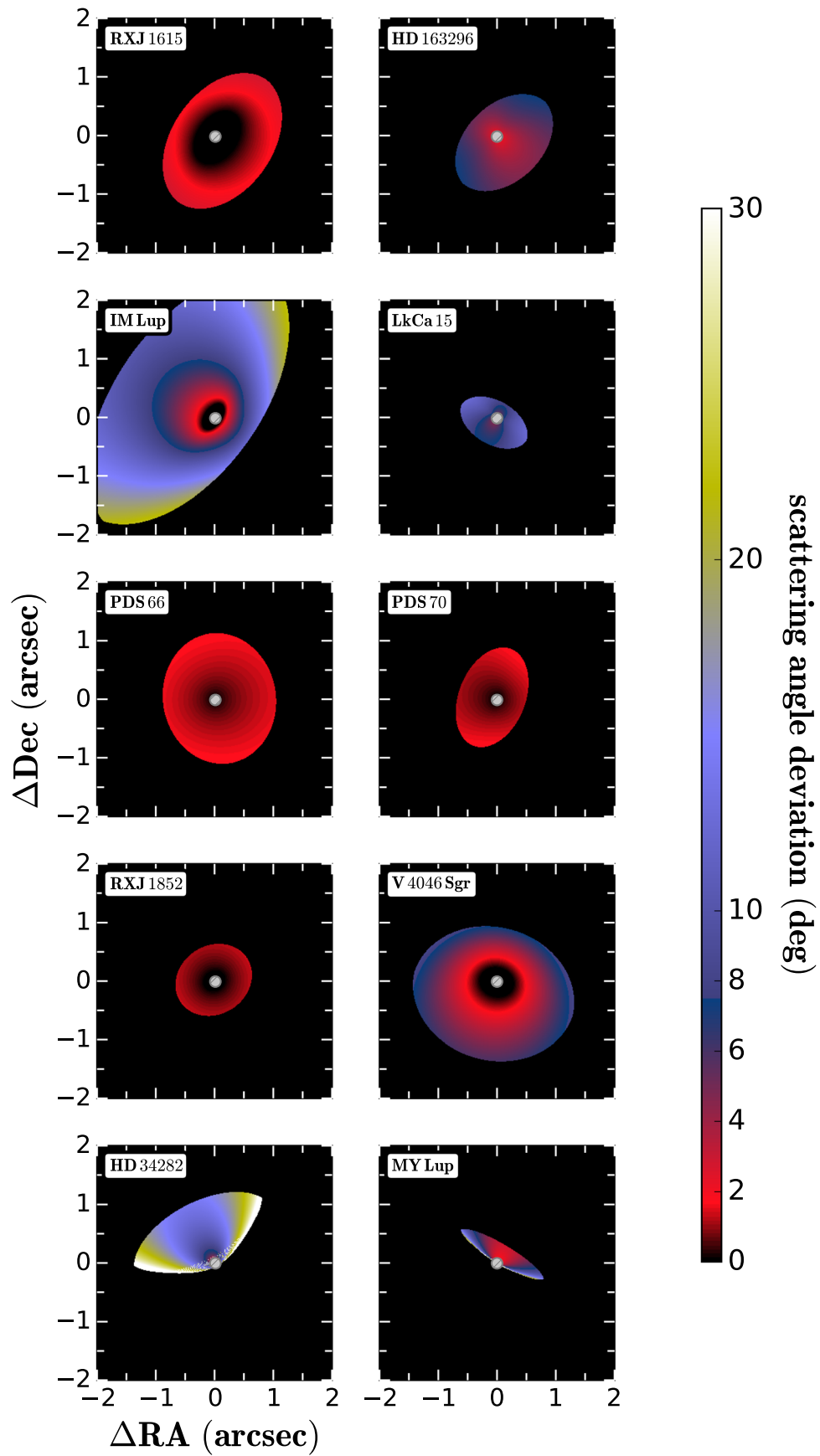


Figure 7. The same as the bottom panel of Figure 1, but for all disks in our sample. Shown are the maximum deviations in scattering angle, based on the flared and the flat surface height profiles.

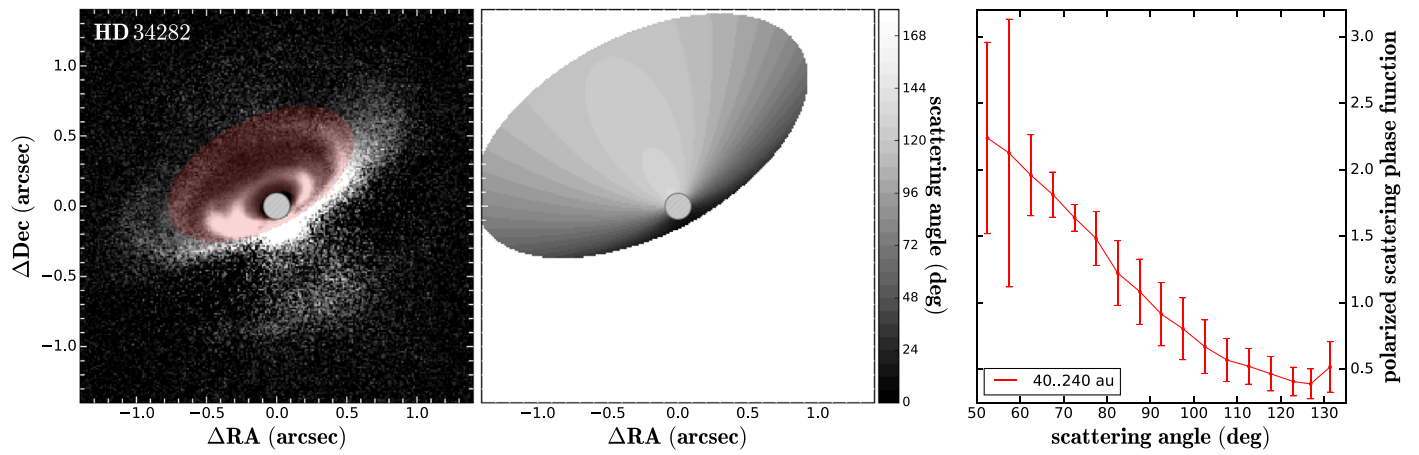


Figure 8. Extracted polarized scattered phase functions and extraction regions for the *J*-band data of the HD 34282 system. The panels are analogous to Figure 2.

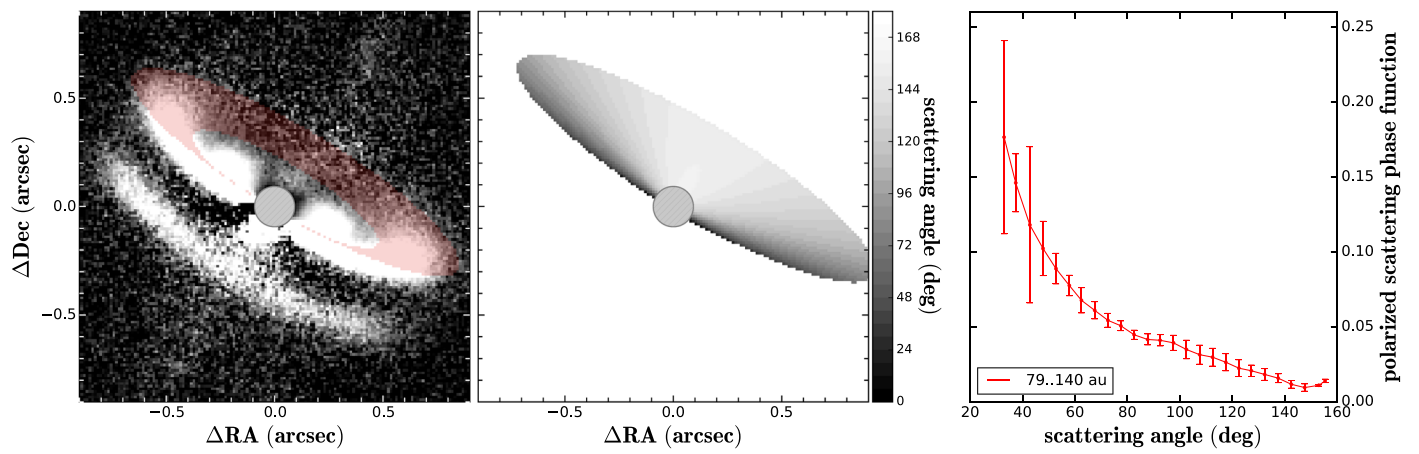


Figure 9. Extracted polarized scattered phase functions and extraction regions for the *H*-band data of the MY Lup system. The panels are analogous to Figure 2.

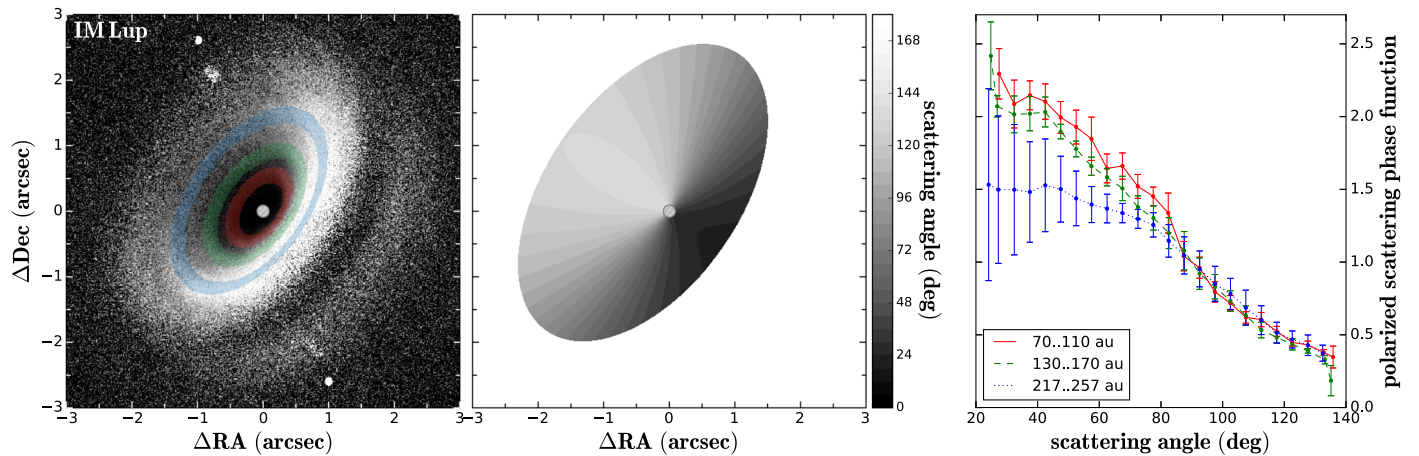


Figure 10. Extracted polarized scattered phase functions and extraction regions for the *H*-band data of the IM Lup system. The panels are analogous to Figure 2. We note that this figure is identical to Figure 1 in Tazaki et al. (2023).

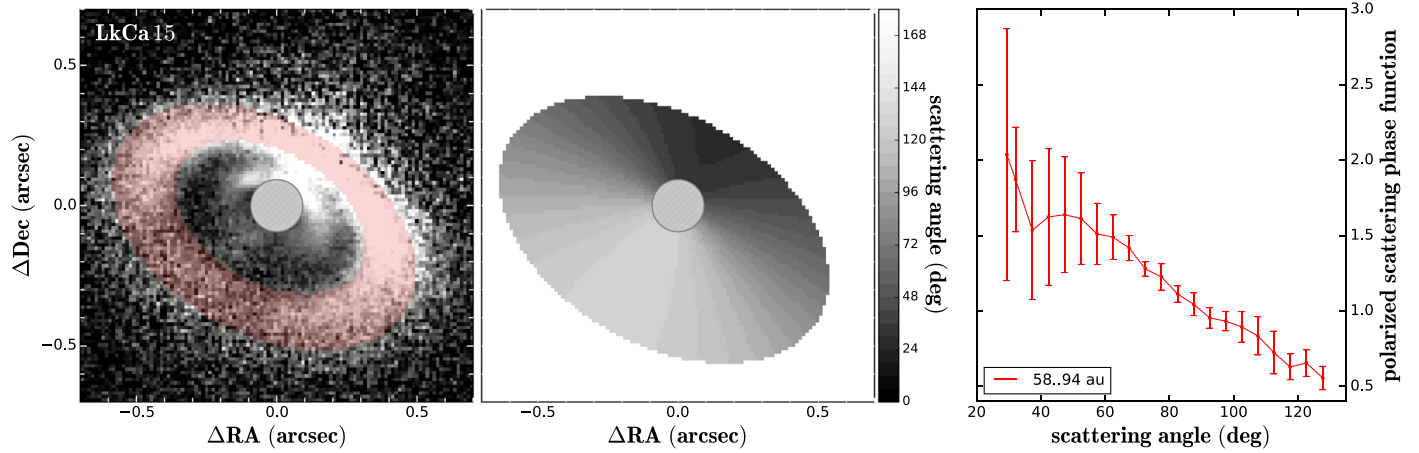


Figure 11. Extracted polarized scattered phase functions and extraction regions for the *J*-band data of the LkCa 15 system. The panels are analogous to Figure 2.

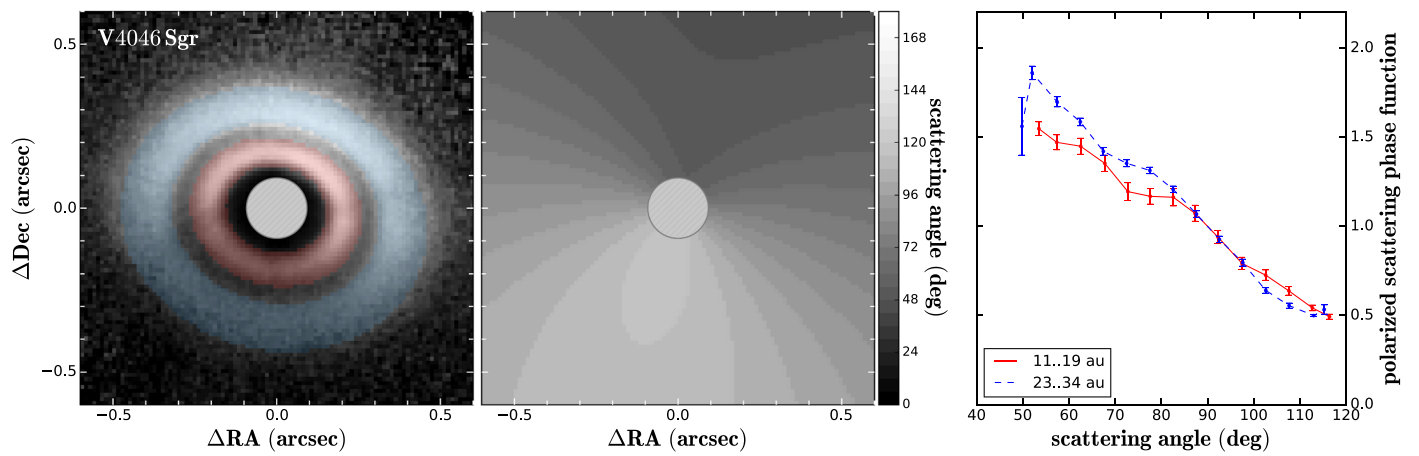


Figure 12. Extracted polarized scattered phase functions and extraction regions for the *H*-band data of the V 4046 Sgr system. The panels are analogous to Figure 2.

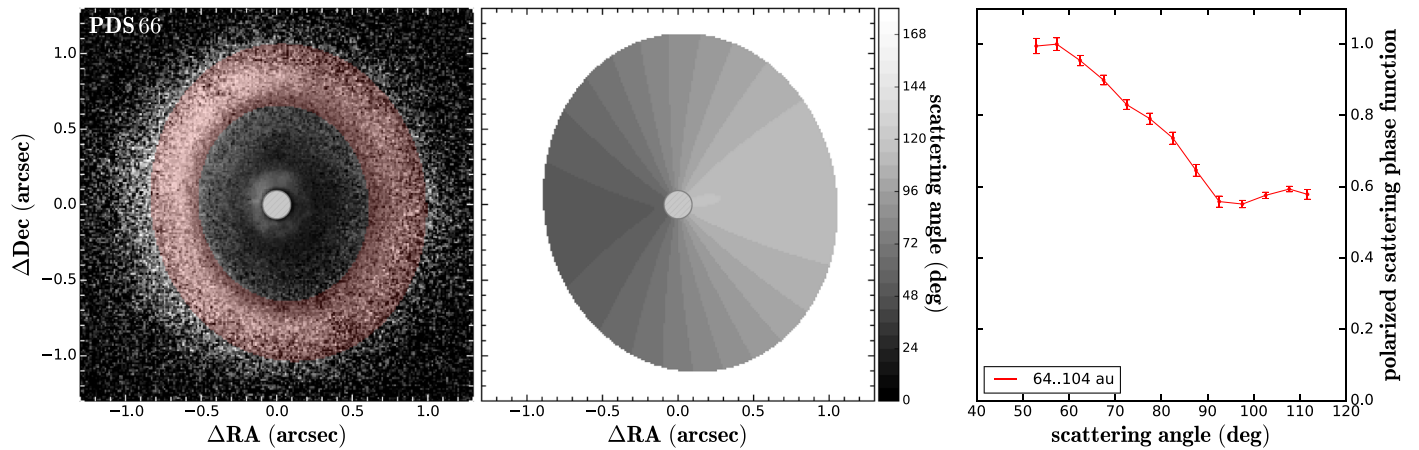


Figure 13. Extracted polarized scattered phase functions and extraction regions for the *H*-band data of the PDS 66 system. The panels are analogous to Figure 2.

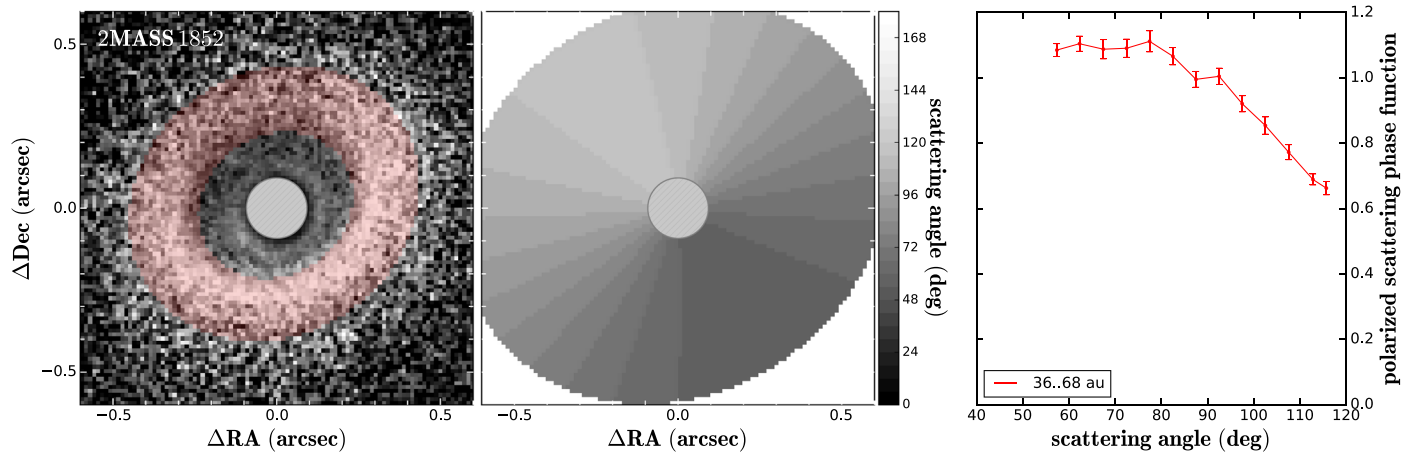


Figure 14. Extracted polarized scattered phase functions and extraction regions for the H -band data of the RXJ 1852 system. The panels are analogous to Figure 2.

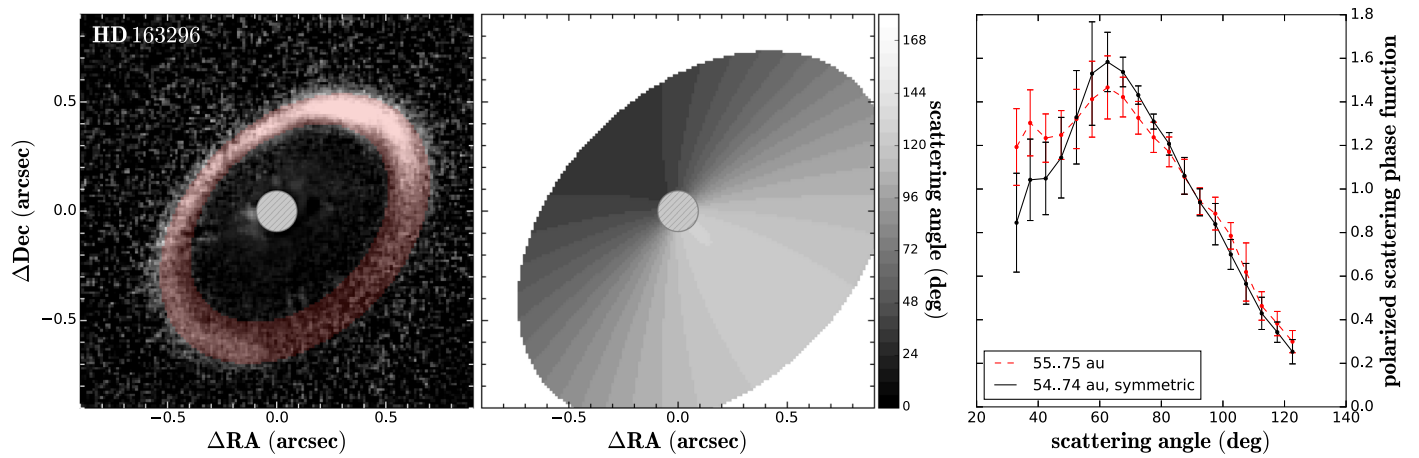


Figure 15. Extracted polarized scattered phase functions and extraction regions for the H -band data of the HD 163296 system. The panels are analogous to Figure 2.

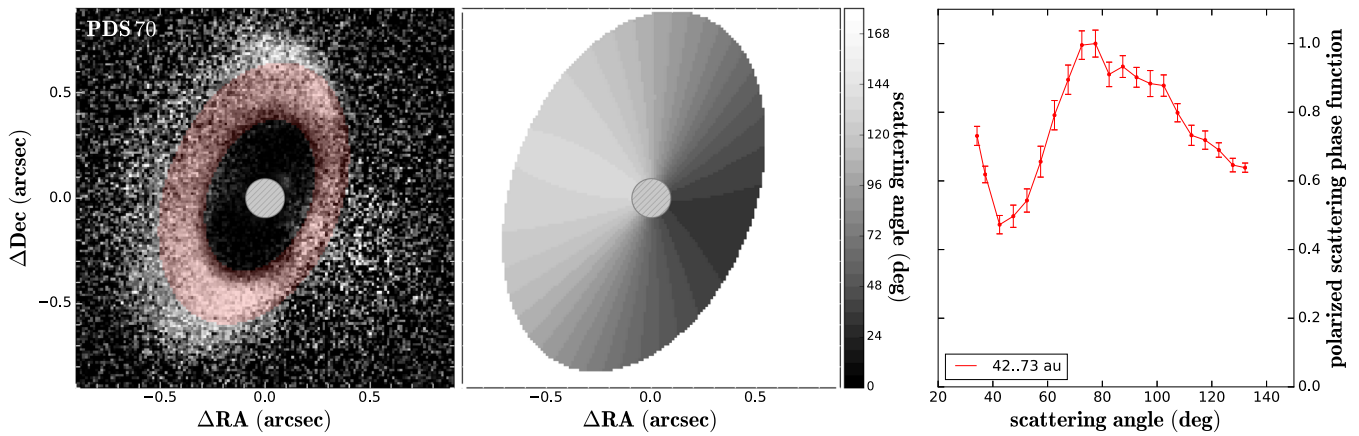


Figure 16. Extracted polarized scattered phase functions and extraction regions for the H -band data of the PDS 70 system. The panels are analogous to Figure 2.

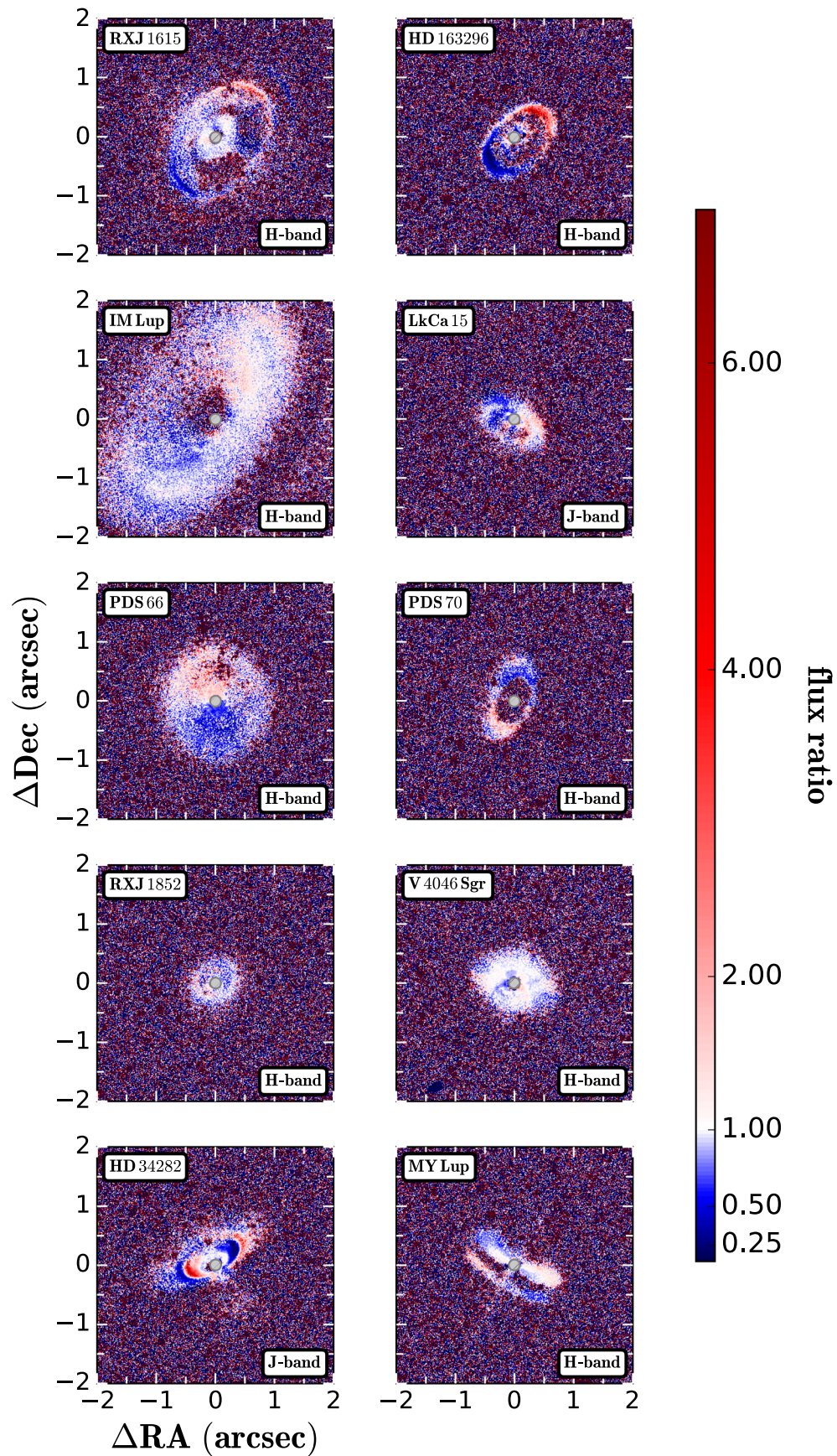


Figure 17. Axis symmetry of all disks in our sample relative to the disk minor axis. *H*-band data are shown when available, otherwise *J*-band data are shown. The disk images were flipped around the minor axis, and then the original image was divided by the flipped image. Thus, flux ratios >1 indicate the factor by which the disk region is brighter than the corresponding axis-symmetric region.

Appendix C

T-matrix Calculations

We considered four different types of dust aggregation: BCCA, BPCA, and two modified versions of BPCA, known as BAM1 and BAM2 (Shen et al. 2008). BCCA has a fractal dimension of 1.9, and therefore has a highly open structure, whereas the other three have a fractal dimension close to 3. The main differences between BPCA, BAM1, and BAM2 are their porosities, with the lowest for BAM2. We assume a spherical and single-sized monomer for computational convenience. Each monomer has a dust composition with a mixture of water ice (Warren & Brandt 2008), pyroxene silicate ($\text{Mg}_{0.7}\text{Fe}_{0.3}\text{SiO}_3$; Dorschner et al. 1995), amorphous carbon (Zubko et al. 1996), and troilite (Henning & Stognienko 1996), with the mass abundance ratios similar to the DSHARP model (Birnstiel et al. 2018). We calculated the effective refractive index (m) by using the Bruggeman mixing rule and found $m = 1.92 + 0.404i$ at a wavelength of $1.63 \mu\text{m}$.





Given dust geometry and composition, we calculate the scattering matrix elements of the dust aggregates by using the Multiple Sphere T-Matrix Method (Mackowski & Mishchenko 2011). In the simulations, we assume that aggregates are randomly oriented, i.e., ignoring grain alignment, and their optical properties were averaged over all possible orientations with equal probability, by using the analytical orientation averaging technique of the T-matrix method. The results were also averaged over four realizations of each aggregate model.

Once we obtain the optical properties for each aggregate, we then average the optical properties by considering the aggregate size distribution:

$$n(a)da \propto a^{-3.5}da \quad (a_{\min} \leq a \leq a_{\max}), \quad (\text{C1})$$

where a is the volume-equivalent radius of an aggregate, defined by $a = a_{\text{mon}}N^{1/3}$, a_{mon} being the radius of the monomer and N being the number of monomers. The minimum aggregate radius is fixed to $a_{\min} = 2a_{\text{mon}}$, and the maximum aggregate radius a_{\max} is a parameter. We consider two different monomer radii: $a_{\text{mon}} = 0.1 \mu\text{m}$ and $0.4 \mu\text{m}$. The largest aggregates we investigated have $a_{\max} = 1.6 \mu\text{m}$. Since the volume-equivalent radius does not necessarily represent the apparent size of an aggregate, we introduce the characteristic radius a_c (Mukai et al. 1992), which better describes the apparent size. We measure the porosity by $\mathcal{P} = 1 - (a/a_c)^3$. The characteristic radius and porosity of the maximum aggregate in the size distribution will be denoted by $a_{c,\max}$ and \mathcal{P}_{\max} , respectively.

ORCID iDs

Christian Ginski  <https://orcid.org/0000-0002-4438-1971>
 Ryo Tazaki  <https://orcid.org/0000-0003-1451-6836>
 Carsten Dominik  <https://orcid.org/0000-0002-3393-2459>
 Tomas Stolker  <https://orcid.org/0000-0002-5823-3072>

References

Alecian, E., Wade, G. A., Catala, C., et al. 2013, *MNRAS*, 429, 1027
 Avenhaus, H., Quanz, S. P., Garufi, A., et al. 2018, *ApJ*, 863, 44
 Avenhaus, H., Quanz, S. P., Schmid, H. M., et al. 2014, *ApJ*, 781, 87
 Astropy Collaboration, Price-Whelan, A. M., Sipőcz, B. M., et al. 2018, *AJ*, 156, 123
 Astropy Collaboration, Robitaille, T. P., Tollerud, E., et al. 2013, *A&A*, 558, A33
 Benisty, M., Dominik, C., Follette, K., et al. 2022, arXiv:2203.09991

Beuzit, J. L., Vigan, A., Mouillet, D., et al. 2019, *A&A*, 631, A155
 Bi, J., Lin, M.-K., & Dong, R. 2021, *ApJ*, 912, 107
 Binkert, F., Szulágyi, J., & Birnstiel, T. 2021, *MNRAS*, 506, 5969
 Birnstiel, T., Andrews, S. M., & Ercolano, B. 2012, *A&A*, 544, A79
 Birnstiel, T., Dullemond, C. P., Zhu, Z., et al. 2018, *ApJL*, 869, L45
 Bohren, C. F., & Huffman, D. R. 1983, *Absorption and Scattering of Light by Small Particles* (New York: Wiley)
 Brauer, F., Dullemond, C. P., & Henning, T. 2008, *A&A*, 480, 859
 Canovas, H., Ménard, F., Hales, A., et al. 2013, *A&A*, 556, A123
 Carillet, M., Bendjoya, P., Abe, L., et al. 2011, *ExA*, 30, 39
 Casassus, S., & Pérez, S. 2019, *ApJL*, 883, L41
 Chiang, E. I., & Goldreich, P. 1997, *ApJ*, 490, 368
 Chiang, E. I., Joungh, M. K., Creech-Eakman, M. J., et al. 2001, *ApJ*, 547, 1077
 Currie, T., Muto, T., Kudo, T., et al. 2014, *ApJL*, 796, L30
 de Boer, J., Ginski, C., Chauvin, G., et al. 2021, *A&A*, 649, A25
 de Boer, J., Langlois, M., van Holstein, R. G., et al. 2020, *A&A*, 633, A63
 de Boer, J., Salter, G., Benisty, M., et al. 2016, *A&A*, 595, A114
 Dohlen, K., Langlois, M., Saisse, M., et al. 2008, *Proc. SPIE*, 7014, 70143L
 Dorschner, J., Begemann, B., Henning, T., Jaeger, C., & Mutschke, H. 1995, *A&A*, 300, 503
 Engler, N., Milli, J., Gratton, R., et al. 2023, *A&A*, 672, A1
 Estrada, P. R., Cuzzi, J. N., & Umurhan, O. M. 2022, *ApJ*, 936, 42
 Garcia, A. J. L., & Gonzalez, J.-F. 2020, *MNRAS*, 493, 1788
 Garufi, A., Avenhaus, H., Pérez, S., et al. 2020, *A&A*, 633, A82
 Garufi, A., Benisty, M., Pinilla, P., et al. 2018, *A&A*, 620, A94
 Garufi, A., Dominik, C., Ginski, C., et al. 2022, *A&A*, 658, A137
 Ginski, C., Facchini, S., Huang, J., et al. 2021, *ApJL*, 908, L25
 Ginski, C., Stolker, T., Pinilla, P., et al. 2016, *A&A*, 595, A112
 Haffert, S. Y., Bohn, A. J., de Boer, J., et al. 2019, *NatAs*, 3, 749
 Hashimoto, J., Dong, R., Kudo, T., et al. 2012, *ApJL*, 758, L19
 Henning, T., & Stognienko, R. 1996, *A&A*, 311, 291
 Herczeg, G. J., & Hillenbrand, L. A. 2014, *ApJ*, 786, 97
 Hunter, J. D. 2007, *CSE*, 9, 90
 Isella, A., Guidi, G., Testi, L., et al. 2016, *PhRvL*, 117, 251101
 Kataoka, A., Tanaka, H., Okuzumi, S., & Wada, K. 2013, *A&A*, 557, L4
 Keppler, M., Benisty, M., Müller, A., et al. 2018, *A&A*, 617, A44
 Kharchenko, N. V. 2001, *KFNT*, 17, 409
 Kobayashi, H., & Tanaka, H. 2021, *ApJ*, 922, 16
 Krijt, S., Ormel, C. W., Dominik, C., & Tielens, A. G. G. M. 2016, *A&A*, 586, A20
 Krolikowski, D. M., Kraus, A. L., & Rizzuto, A. C. 2021, *AJ*, 162, 110
 Lorek, S., Lacerda, P., & Blum, J. 2018, *A&A*, 611, A18
 Luhman, K. L. 2022, *AJ*, 163, 24
 Mackowski, D. W., & Mishchenko, M. I. 2011, *JQSRT*, 112, 2182
 Marino, S., Perez, S., & Casassus, S. 2015, *ApJL*, 798, L44
 Martinez-Brunner, R., Casassus, S., Pérez, S., et al. 2022, *MNRAS*, 510, 1248
 McCabe, C., Duchêne, G., & Ghez, A. M. 2002, *ApJ*, 575, 974
 Milli, J., Engler, N., Schmid, H. M., et al. 2019, *A&A*, 626, A54
 Milli, J., Vigan, A., Mouillet, D., et al. 2017, *A&A*, 599, A108
 Min, M., Hovenier, J. W., & de Koter, A. 2005, *A&A*, 432, 909
 Minato, T., Köhler, M., Kimura, H., Mann, I., & Yamamoto, T. 2006, *A&A*, 452, 701
 Monnier, J. D., Harries, T. J., Bae, J., et al. 2019, *ApJ*, 872, 122
 Mukai, T., Ishimoto, H., Kozasa, T., Blum, J., & Greenberg, J. M. 1992, *A&A*, 262, 315
 Mulders, G. D., Min, M., Dominik, C., Debes, J. H., & Schneider, G. 2013, *A&A*, 549, A112
 Mulders, G. D., Pascucci, I., Manara, C. F., et al. 2017, *ApJ*, 847, 31
 Müller, A., Keppler, M., Henning, T., et al. 2018, *A&A*, 617, L2
 Muro-Arena, G. A., Benisty, M., Ginski, C., et al. 2020, *A&A*, 635, A121
 Muro-Arena, G. A., Dominik, C., Waters, L. B. F. M., et al. 2018, *A&A*, 614, A24
 Okuzumi, S., Tanaka, H., Kobayashi, H., & Wada, K. 2012, *ApJ*, 752, 106
 Oliphant, T. E. 2006, *A Guide to NumPy*, Vol. 1 (Austin, TX: Trelgol Publishing)
 Olofsson, J., Milli, J., Bayo, A., Henning, T., & Engler, N. 2020, *A&A*, 640, A12
 Ormel, C. W., Spaans, M., & Tielens, A. G. G. M. 2007, *A&A*, 461, 215
 Pecaat, M. J., & Mamajek, E. E. 2013, *ApJS*, 208, 9
 Pecaat, M. J., & Mamajek, E. E. 2016, *MNRAS*, 461, 794
 Pinte, C., Price, D. J., Ménard, F., et al. 2018, *ApJL*, 860, L13
 Quanz, S. P., Amara, A., Meyer, M. R., et al. 2013, *ApJL*, 766, L1
 Quanz, S. P., Schmid, H. M., Geissler, K., et al. 2011, *ApJ*, 738, 23
 Rich, E. A., Monnier, J. D., Aarnio, A., et al. 2022, *AJ*, 164, 109
 Sartori, M. J., Lépine, J. R. D., & Dias, W. S. 2003, *A&A*, 404, 913
 Shen, Y., Draine, B. T., & Johnson, E. T. 2008, *ApJ*, 689, 260
 Stapper, L. M., Hogerheijde, M. R., van Dishoeck, E. F., & Mentel, R. 2022, *A&A*, 658, A112

- Stolker, T., Dominik, C., Avenhaus, H., et al. 2016, *A&A*, 595, A113
- Szulágyi, J., Binkert, F., & Surville, C. 2022, *ApJ*, 924, 1
- Tamura, M. 2016, *PJAB*, 92, 45
- Tazaki, R. 2021, *MNRAS*, 504, 2811
- Tazaki, R., & Dominik, C. 2022, *A&A*, 663, A57
- Tazaki, R., Ginski, C., & Dominik, C. 2023, *ApJL*, 944, L43
- Tazaki, R., Murakawa, K., Muto, T., Honda, M., & Inoue, A. K. 2021, *ApJ*, 921, 173
- Tazaki, R., Tanaka, H., Muto, T., Kataoka, A., & Okuzumi, S. 2019, *MNRAS*, 485, 4951
- Tazaki, R., Tanaka, H., Okuzumi, S., Kataoka, A., & Nomura, H. 2016, *ApJ*, 823, 70
- Teague, R., Bae, J., Bergin, E. A., Birnstiel, T., & Foreman-Mackey, D. 2018, *ApJL*, 860, L12
- Thalmann, C., Janson, M., Garufi, A., et al. 2016, *ApJL*, 828, L17
- Thalmann, C., Mulders, G. D., Hodapp, K., et al. 2014, *A&A*, 566, A51
- van der Marel, N., Dong, R., di Francesco, J., Williams, J. P., & Tobin, J. 2019, *ApJ*, 872, 112
- van der Marel, N., & Mulders, G. D. 2021, *AJ*, 162, 28
- van Holstein, R. G., Girard, J. H., de Boer, J., et al. 2020, *A&A*, 633, A64
- Villenave, M., Benisty, M., Dent, W. R. F., et al. 2019, *A&A*, 624, A7
- Virtanen, P., Gommers, R., Oliphant, T. E., et al. 2020, *NatMe*, 17, 261
- Wahhaj, Z., Cieza, L., Koerner, D. W., et al. 2010, *ApJ*, 724, 835
- Warren, S. G., & Brandt, R. E. 2008, *JGRD*, 113, D14220
- Wenger, M., Ochsenbein, F., Egret, D., et al. 2000, *A&AS*, 143, 9
- Zsom, A., Ormel, C. W., Güttler, C., Blum, J., & Dullemond, C. P. 2010, *A&A*, 513, A57
- Zubko, V. G., Mennella, V., Colangeli, L., & Bussoletti, E. 1996, *MNRAS*, 282, 1321